The effect of stress barriers on unconventional-singularity-driven frictional rupture

Barnaby Fryer, Mathias Lebihain, Corentin Noël, Federica Paglialunga, François Passelègue

Highlights

The effect of stress barriers on unconventional-singularity-driven frictional rupture

Barnaby Fryer, Mathias Lebihain, Corentin Noël, Federica Paglialunga, François Passelègue

- Stress barriers promote rupture arrest by decreasing energy flux to the crack tip
- Long-tailed frictional weakening must be included in LEFM to predict crack arrest
- This long-tailed weakening depends on the in-situ stress conditions
- Fault preconditioning is experimentally demonstrated to contain dynamic events

The effect of stress barriers on unconventional-singularity-driven frictional rupture

Barnaby Fryer[a], Mathias Lebihain[b], Corentin Noël[a], Federica Paglialunga[a], François Passelègue[a]

[a] *Université Côte d'Azur, CNRS, Observatoire de la Côte d'Azur, IRD, Géoazur, Valbonne, France*
[b] *Laboratoire Navier, CNRS (UMR 8205), École des Ponts ParisTech, Université Gustave Eiffel, Champs-sur-Marne, France*

Abstract

Whether or not energy dissipation is localized in the vicinity of the rupture tip, and whether any distal energy dissipation far from the crack tip has a significant influence on rupture dynamics are key questions in the description of frictional ruptures, in particular regarding the application of Linear Elastic Fracture Mechanics (LEFM) to earthquakes. These questions are investigated experimentally using a 40-cm-long experimental frictional interface. Three independent pistons apply a normal load with a fourth piston applying a shear load, enabling the application of a heterogeneous stress state and stress barriers. After loading the frictional interface to a near-critical state, subsequent unloading of one normal-load piston leads to dynamic ruptures which propagate into the heterogeneous stress fields. The ruptures in these experiments are found to be driven by unconventional singularities, characterised by an ever-increasing breakdown work with slip, and as a result do not conform to the assumptions of LEFM. As these experimental stress barriers inhibit slip, they therefore also reduce the breakdown work occurring outside of the cohesive zone. It is shown that this distal weakening, far from the crack tip, must be considered for the accurate prediction of rupture arrest length. These experiments are performed in the context of a proposed stimulation technique for Enhanced Geothermal Systems (EGSs). It has previously been suggested, through theoretical arguments, that stress barriers could be induced through the manipulation of pore pressure such that there is reduced seismic hazard during the shear stimulation of EGSs. This stimulation technique, known as preconditioning, is demonstrated here to reduce the mechanical energy flux to the crack tip, G, while also increasing the fracture energy, G_c. Preconditioning is shown to be capable of arresting seismic rupture and reducing co-seismic slip, slip velocity, and seismic moment at preconditioning stresses which are reasonably achievable in the field. Due to the fully-coupled nature of seismic rupture and fault slip, preconditioning also reduces distal weakening and its contribution to the propagation of induced seismic ruptures. In a similar vein, heterogeneous pore pressure fields associated with some seismic swarms can be used to explain changes in stress drop within the swarm without recourse to material or total-stress heterogeneity.

Keywords: Frictional ruptures, Stress barriers, Rupture dynamics, Unconventional singularity, Preconditioning

*Corresponding author: barnaby.fryer@geoazur.unice.fr

1. Introduction

The injection of fluid into the subsurface has been associated with induced seismicity on a significant number of occasions. These injection operations have had a variety of purposes, such as fluid disposal/storage, improved hydrocarbon recovery (e.g., Raleigh et al. (1976)), and reservoir stimulation (e.g., Bao and Eaton (2016)). In the case of reservoir stimulation for Enhanced Geothermal Systems (EGSs), the mechanical stimulation of a fault or fracture zone is, in theory, achieved through the induced shear dilation of the targeted discontinuity (e.g., Lee and Cho (2002)). The shearing itself is induced through the increase in pore pressure associated with fluid injection, which acts to reduce the fault's effective normal stress and initiate shear failure. Ideally, this process occurs aseismically, such that seismic waves are not radiated. However, as injection continues, the rupture front bounding the stimulated region grows, potentially surpassing the area of increased pore pressure if the fault is critically stressed (Garagash and Germanovich, 2012; Bhattacharya and Viesca, 2019; Cebry and McLaskey, 2021). Eventually, this rupture front may reach a critical length, known as the nucleation length (Ida, 1972; Okubo and Dieterich, 1984; Campillo and Ionescu, 1997; Uenishi and Rice, 2003), and begin accelerating, resulting in the dynamic rupture of the fault and the radiation of potentially-damaging seismic waves. The understanding of how to achieve shear dilation in an aseismic manner while avoiding the dynamic rupture of the fault is an obstacle for the global development of EGSs, and a number of field-scale EGS projects have been impeded or halted due to the seismicity they have induced (e.g., Basel, Switzerland (Häring et al., 2008); Pohang, South Korea (Kim et al., 2018)).

The success or failure of an EGS operation is strongly dependent on the state of stress in the subsurface. This is because the state of stress not only influences the susceptibility of a given fault to shear dilation (e.g., Lee and Cho (2002)), but also affects the nucleation length (Okubo and Dieterich, 1984), rupture velocity (Ben-David et al., 2010), slip velocity (Okubo and Dieterich, 1984), rupture halting (Husseini et al., 1975), and radiated seismic energy (Scholz, 1968) of earthquakes. In particular, recent experimental and theoretical studies have highlighted that the rupture length, i.e., the size of the earthquake that will eventually be induced, is contingent upon the stress distribution along the fault (Bayart et al., 2016; Galis et al., 2017). Indeed, rupture arrest is described by the flux of total potential energy per unit extension of the crack tip (commonly termed G) and the dissipated energy related to the unit extension of the crack tip (commonly termed G_c or fracture energy); both of these terms depend on the stress state. It is generally assumed that weakening is localized near the crack tip, such that, while slip may continue, there is no further weakening once slip has reached a critical slip distance, allowing the stress and strain fields around the crack tip to be described by a conventional singularity. However, recently, instances of continued power-law weakening beyond this critical slip distance have been observed experimentally, resulting in unconventional singular stress and strain fields (Paglialunga et al., 2024). This raises the question as to whether or not the energy release rate and, therefore rupture arrest, are truly governed exclusively by near-tip weakening (Garagash, 2021; Brener and Bouchbinder, 2021b; Kammer et al., 2024). It is further unclear what effect, if any, stress barriers and the stress state in general have on distal weakening and if a reduction in distal weakening promotes rupture arrest.

Engineering operations are capable of influencing the state of stress in the Earth's crust. For example, fluid production was first connected to land subsidence nearly a century ago (Pratt and Johnson, 1926), and fluid injection was linked to seismicity in the 1960's and 1970's (Raleigh et al., 1976). Concurrently, in the oil and gas industry, operators began actively manipulating the *in-situ* stress with hydraulic fracturing operations, first employed in the 1940's (Clark, 1949),

which rely on the reduction of the minimum principal effective stress through the increase of fluid pressure (Hubbert and Willis, 1957). Later, operators began recognizing that the *in-situ* stress could be manipulated prior to initiating a hydraulic fracture for that fracture's eventual benefit (Shuck, 1977).

Similarly, the mining industry has been employing a de-stressing technique referred to as preconditioning since the 1950's (Roux et al., 1957). In this operation, a rock face is artificially fractured in order to relieve stress and reduce the occurrence and severity of rockbursts. Still in its relative infancy, the EGS industry has not sufficiently developed methods to reduce the hazard of induced seismic events related to stimulation operations. However, the potential to direct and inhibit stimulation treatments by manipulating pore pressure has been recognized for two decades already (Baria et al., 2004), and methodologies to inhibit the occurrence of large seismic events such as cyclic stimulation/fatigue hydraulic fracturing (Zimmermann et al., 2010; Zang et al., 2013; Hofmann et al., 2019; Noël et al., 2019), control theory (Stefanou and Tzortzopoulos, 2022), fracture caging (Frash et al., 2021), and preconditioning (Fryer et al., 2020, 2023; Jalali et al., 2023) have been suggested, developed, and, in the case of cyclic stimulation, even deployed at the field scale.

Here, using the effective stress principle, the preconditioning of an EGS through the development of stress barriers (Fryer et al., 2023) is demonstrated experimentally using a biaxial apparatus. In practice these stress barriers are proposed to be achieved through an extended (but short compared to the background stressing rate) period of production, reducing pore pressure and increasing effective stress, prior to a comparatively-shorter period of injection, stimulating the fault by inducing slip, Figure 1(a-c). Here, this procedure will be simulated in dry conditions with changes in total normal stress, Figure 1(d,e). It is shown that preconditioning has the capability to halt nucleated dynamic ruptures, reducing the hazard associated with fluid injection into a fault. Preconditioning achieves this moderation in hazard through the abatement of energy available to the propagating rupture via a diminished stress drop and the increase in the energy required to continue dynamic propagation via an increased fracture energy; in accordance with previous findings and predictions (Husseini et al., 1975; Freund, 1990; Kammer et al., 2015; Bayart et al., 2016; Galis et al., 2017; Bayart et al., 2018; Gvirtzman and Fineberg, 2021; Cebry et al., 2022; Fryer et al., 2023; Barras et al., 2023). Further, it will be shown that distal weakening, far from the crack tip, exhibits a first-order control on rupture arrest and is also reduced by preconditioning and stress barriers in general.

2. Methods

2.1. Experimental Setup

The biaxial apparatus, CrackDyn, located at Géoazur in Valbonne, France, was used to perform experiments on two polymethylmethacrylate (PMMA) rectangular-prism blocks ($40 \times 10 \times 1$ cm and $45 \times 10 \times 1.8$ cm), yielding a fault length, L, of 40 cm and a fault width of 1 cm, Figure 1(f). The position of any point along the sample is given by its horizontal, x, and vertical, y, coordinates. The apparatus engages with the sample blocks via three independent vertical pistons, responsible for applying normal forces, and one horizontal piston, responsible for applying a shearing force. The pistons are driven with two ENERPAC P141 hydraulic pumps and transmit load to the sample blocks via steel sample holders. The sample holders transmitting the normal stress to the fault system are discontinuous, allowing for a heterogeneous normal load to be applied along the fault length, Figure 1f. The force applied by each piston is recorded at 500 Hz by

a Scaime K13 load cell located in between it and the sample holder. Thirteen 350-Ohm strain-gauge rosettes (39 total strain gauges), recording at 2 MHz, are glued at 3 mm from the simulated fault interface. The strain gauges' signals are amplified by a factor of 100 by Elsys SGA-2 MK2 amplifiers. Twenty Brüel & Kjær type 8309 accelerometers are glued either horizontally or vertically at approximately 1 cm from the simulated fault interface and record at 2 MHz with a cutoff frequency of 54 kHz. Finally, three high-intensity light sources emit light which traverses the sample to arrive at a Phantom TMX 6410 high-speed camera. The light is cross-polarized with two linear polarizing filters. During the experiments, the camera was triggered using a piezoelectric sensor and recorded frames at 500 kHz (1.7 μsec exposure time with a 1280×32 pixel resolution across the fault length, i.e., 350 μm per pixel). The high-speed camera and the use of polarized light with a birefringent material allow for the use of photoelasticity, which enables the tracking any propagating dynamic ruptures (Rosakis et al., 1999; Nielsen et al., 2010; Schubnel et al., 2011; Latour et al., 2013; Gounon et al., 2022; Paglialunga et al., 2023). The piezoelectric sensor signal used for the camera triggering was split between the recording computers and used to synchronize the different recording systems. The data treatment is addressed in the appendix A.

2.2. Experimental Approach

The sample is loaded in steps, Figure 1(d,e), by increasing the normal stress and shear stress applied at the pistons in increments of 30 bar. After initial loading, the normal stresses applied by all three vertical pistons are equivalent and set to either 60, 90, or 120 bar nominal normal stress, σ^0, i.e., as read on the pump's analogue gauge in the hydraulic pressure lines. The shear stress is set to a value just below the shear stress required to initiate a dynamic event, in this case corresponding to 100, 145, or 190 bar nominal shear stress. The volume at the shear pump was then maintained constant for the rest of the experiment. At this stage the sample fault is considered to be loaded and representative of a tectonically-loaded natural fault, Figure 1a. If the sample is to be preconditioned, the normal stress applied by all three vertical pistons is increased by a nominal normal stress of $\Delta\sigma^{\mathrm{p}}$, such that $\frac{\Delta\sigma^{\mathrm{p}}}{\sigma^0}$ is equivalent to approximately 0.08, 0.16, or 0.24, Figure 1(b,d). In practice, if the normal total stress on a fault is given by a lithostatic gradient of 23 $\frac{\mathrm{MPa}}{\mathrm{km}}$ and the pore pressure by a hydrostatic gradient of 10 $\frac{\mathrm{MPa}}{\mathrm{km}}$, these values of $\frac{\Delta\sigma^{\mathrm{p}}}{\sigma^0}$ correspond to producing fluid from the fault such that the effective hydrostatic gradient on the fault is reduced to approximately 9, 8, or 7 $\frac{\mathrm{MPa}}{\mathrm{km}}$. At each normal stress a base case is also tested twice whereby the stress is not preconditioned and $\frac{\Delta\sigma^{\mathrm{p}}}{\sigma^0} = 0$, serving as reference. Injection is then simulated by reducing the stress applied by the right-hand-side vertical piston (closest to the horizontal piston), leaving the other two vertical pistons applying the preconditioned stress, Figure 1(d-f). The unloading generally results in an audible acoustic event, after which the shear and then normal stresses are unloaded and the sample reset.

3. Experimental Results

The local stress recorded by the strain gauge rosettes show that the stress profiles are highly reproducible between experiments, Figure 2. The strain gauges show that preconditioning increases the normal stress, σ_{yy}, with smaller changes to shear stress, σ_{xy}. Strain gauge measurements were further able to provide stress profiles just before and just after the nucleation of the principal dynamic event associated with each experiment, Figure 2.

The stress-induced birefringence of the PMMA samples allows for photoelasticity measurements, which provide a second independent method to track the propagating ruptures. When

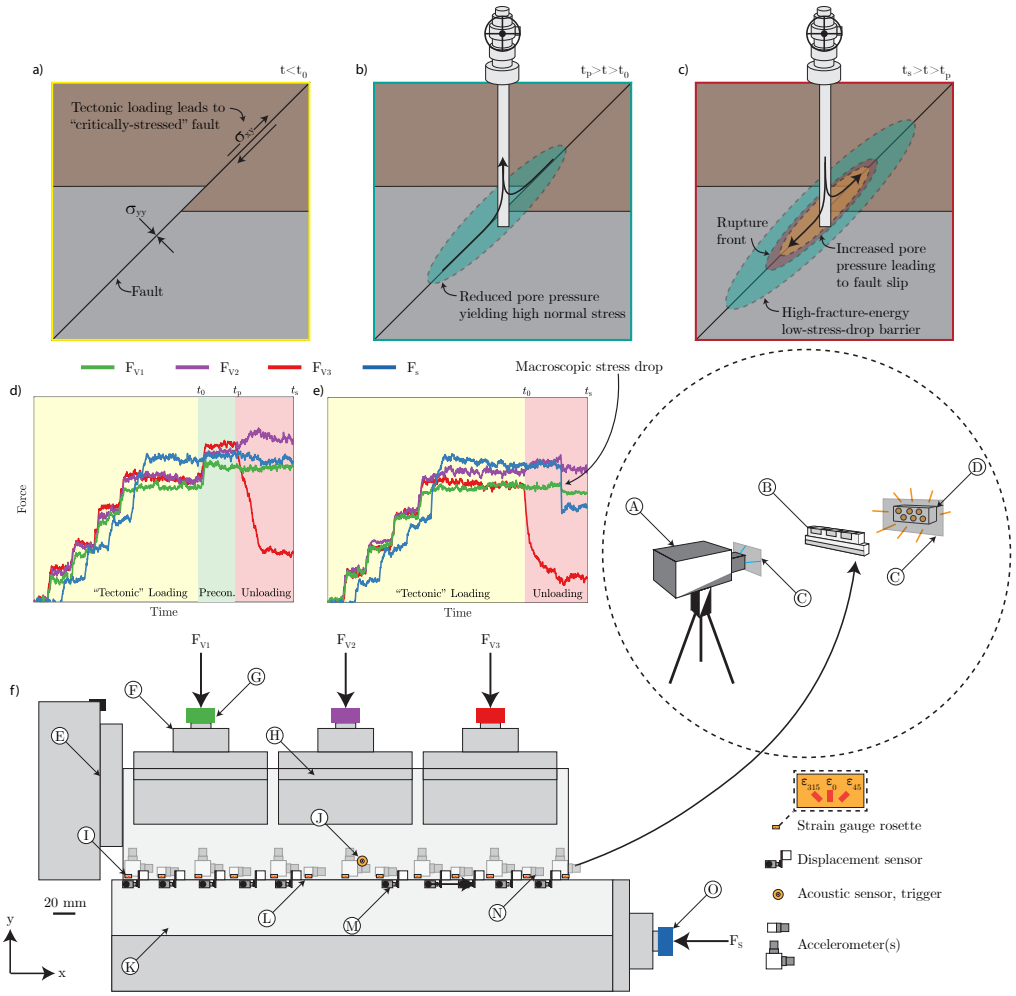

Figure 1: An overview of preconditioning and the experimental procedure. (a-c) illustrates preconditioning as it could be applied at the field scale, with the process simulated in the laboratory here under dry conditions. (a) Tectonic loading results in a critically-stressed fault at depth. (b) A well is drilled into the fault. Fluid is produced from the fault, reducing the pore pressure and increasing the effective normal stress. (c) Fluid is injected into the fault on a time scale significantly shorter than the production phase in (b). The increased pore pressure locally reduces the effective stress and initiates slip. This slipping or rupture front may outpace the fluid pressure front, but will encounter the low-pore-pressure region, which acts as a fracture-energy and reduced-shear-stress-drop barrier (Fryer et al., 2023). In the context of this figure, t is time, t_0 is the start of operations, t_p is the time when fluid production stops, and t_s is the time of shut-in. (d,e) The stress profiles of two example experiments, illustrating the left-most vertical load (green), central vertical load (purple), right-most vertical load (red), and shear load (blue). Initially, the normal and shear loads are increased, simulating tectonic loading (a). If preconditioning is applied (b,d), the vertical loads are increased. In the case preconditioning is not applied, this step is skipped (e). The right-most vertical load is then reduced, simulating fluid injection. This results in the nucleation of a dynamic rupture. Note the macroscopic stress drop present in the non-preconditioned case (e). This macroscopic stress drop is not present in the preconditioned case (d) and is the first piece of evidence suggesting that the preconditioned case halted rupture propagation, containing the event, whereas the non-preconditioned case ruptured the entire experimental fault, reaching the sample edges and resulting in reduced stiffness and extra slip (e.g., Kilgore et al. (2017)). (f) The experimental setup with the inset showing the camera setup. (A) high-speed camera, (B) biaxial setup, (C) linear polarizer, (D) light source, (E) stopper, (F) load cell, (G) vertical piston, (H) sample holder, (I) strain gauge rosette, (J) acoustic sensor (trigger), (K) PMMA sample, (L) sample-sample interface, (M) displacement sensor (only in Supplementary Material), (N) accelerometer, and (O) horizontal piston.

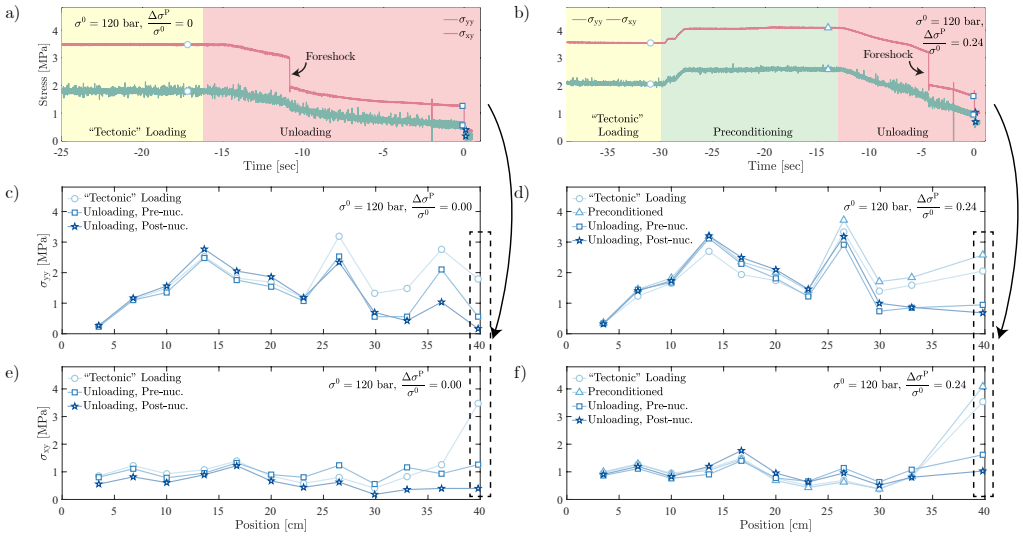

Figure 2: Stress profiles deduced from strain gauge measurements for two experiments performed at a nominal normal stress of 120 bar. (a,c,e) No preconditioning is performed. (b,d,f) A preconditioning of 30 bar is applied. (a,b) The stress profile in time found from one strain gauge located at a position near the sample edge (x = 40 cm), in the area where the sample is unloaded. The initial normal (green) and shear (red) stresses, representative of the *in-situ* stress resulting from tectonic loading have a yellow background. The unloading phase has a red background. In (b) the preconditioning phase has a green background. Note both experiments have a foreshock during the unloading phase which is contained on one side of the sample. The normal (c,d) and shear (e,f) stress profiles across the entire surface of the sample, using all working strain gauges at specific moments: after "tectonic" loading (circle), after preconditioning (triangle), during unloading but prior to the dynamic event (square), and after the dynamic event (star). Markers represent values found from the strain gauges. Lines are linear interpolations. Note the similarities in the initial stress profiles (circles) between the two cases. Additionally, note the stress increase in (d,f) related to preconditioning (triangles). Finally, note the reduced shear stress in (e) after the event across the entirety of the sample (stars). The shear stress is increased in the preconditioned case (f). The case without preconditioning resulted in the rupturing of the entire sample; the preconditioned case had a contained event.

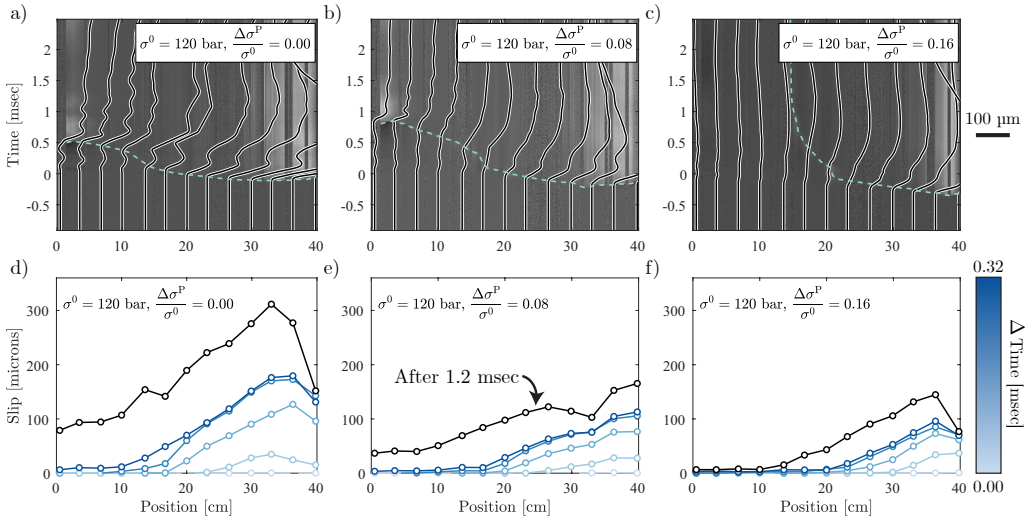

Figure 3: Three experiments are shown, all performed at a nominal normal stress of 120 bar. (a,d) No preconditioning is performed. (b,c,e,f) Preconditioning is performed up to a nominal normal stress of (b,e) 130 and (c,f) 140 bar. (a-c) The videogram profiles illustrate the progression of the rupture fronts and are overlain by the local displacement recorded by the horizontally-oriented accelerometers (black lines). The displacements are zeroed to the location of the sensor and deviation from this position indicates local displacement. The scale for the displacement is found on the right. The rupture front is traced with a dotted line. Note that certain spatial bands where the grey-scale remains uniform on the videograms correspond to areas where light was not able to pass through the sample at the height of the fault. This is due to it being blocked by a sensor. (d-f) The slip profiles as calculated from the accelerometers positioned along the fault interface. An initial time, here denoted by the color bar as 0.00 microseconds, is chosen just before slip initiates. Then, four additional evenly-spaced times are taken starting from this moment at 0.08, 0.16, 0.24, and 0.32 microseconds. The "final" slip profile after 1.2 microseconds is shown in black. The positions of the accelerometers are denoted by white circles, with linear interpolation between these points.

these measurements are taken in combination with the slip profiles, computed from the accelerometers, the rupture fronts of the dynamic events can be traced, Figure 3(a-c). Measurements of slip were used to build slip profiles across the fault interface, Figure 3(d-f). The slip profiles show that the larger the magnitude of the preconditioning, the smaller the total cumulative slip and slip velocities are. Note finally that the characteristic rise times (slip durations) computed by the accelerometers are similar to the characteristic source durations (the time required for the rupture to traverse the sample) observed on the videograms, meaning that these ruptures exhibit crack-like, as opposed to pulse-like, behaviour.

Preconditioning results in halted and/or slowed rupture and reduced slip, slip velocity, stress drop, and moment magnitude, Figures 3 and 4. The videogram measurements were manually traced, allowing for the creation of rupture profiles for the dynamic events associated with each experiment, Figure 4(a-c). In all cases where preconditioning was not applied, the rupture was able to traverse the entire interface, highlighting that, while the stress state along the interface is heterogeneous (all ruptures experienced deceleration at approximately x = 15 cm, presumably associated with a higher normal stress at this position, Figure 2(c,d)), on the whole the tested conditions can be considered representative of a critically-stressed fault. However, with the exception of one experiment ($\sigma^0 = 120$ bar; $\frac{\Delta\sigma^P}{\sigma^0} = 0.08$), preconditioning was able to halt the dynamically-propagating rupture before it reached the sample edges at all tested nominal normal

stresses (σ^0 = 60, 90, and 120 bar) and all tested levels of preconditioning ($\frac{\Delta\sigma^P}{\sigma^0}$ = 0.08, 0.16, 0.24). This result is further confirmed by the slip profiles, Figure 4(d-f). Generally, although the results are influenced by whether or not the rupture reaches the free boundary at the sample edges (Kilgore et al., 2017), preconditioning results in reduced total slip behind the crack tip and reduced slip velocity, Figure 4(d-i). In fact, the accelerometers provide a near-continuous measure of slip along the interface that can be used to estimate the seismic moment, M_0, of each event as $M_0 = \mu A_s D$ (Aki, 1966), where μ is the dynamic shear modulus, D is the slip, and A_s the area of the ruptured region along the interface. Without preconditioning, experiments with nominal normal stresses of 60, 90, and 120 bar yield average seismic moments of 416, 940, and 1608 N·m, respectively. With a preconditioning of $\frac{\Delta\sigma^P}{\sigma^0}$ = 0.24, experiments with nominal normal stresses of 60, 90, and 120 bar yield seismic moments of 86, 474, and 495 N·m, respectively, corresponding to a 50 to 79% reduction in seismic moment due to preconditioning. Finally, strain gauge measurements from before and after the passing of the rupture front allow for the calculation of a continuous stress drop profile, Figure 4(j-l). Preconditioning results in smaller stress drops behind the rupture front, as well as negative stress drops (increases in shear stress) in the cases that it is able to halt the propagating rupture. The stress drop profile, $\Delta\sigma_{xy}$ (x), will later be seen to be of importance for the energy flux reaching the crack tip of the propagating rupture.

4. Discussion

4.1. Fault preconditioning for reduced hazard during EGS stimulation

During crack propagation, the mechanical energy release rate, or the flux of total potential energy per unit extension of a crack's tip, G, is equivalent to the dissipated energy related to that same unit extension, which is known as the fracture energy, G_c, such that (Griffith, 1921; Freund, 1990),

$$G = G_c. \tag{1}$$

The arrest of a dynamically-propagating shear crack can occur due to an increase in G_c or a reduction in G, such that G falls below G_c (Husseini et al. (1975); Rice (1980), page 594; Freund (1990), Eqn. 7.4.27; Kammer et al. (2015); Bayart et al. (2016)).

In this context, fault preconditioning results in a reduction in the energy available to a propagating rupture and in a fracture energy barrier (Fryer et al., 2023). These predictions are based on and in agreement with Linear Elastic Fracture Mechanics (LEFM) theory (Husseini et al., 1975; Rice, 1980; Freund, 1990; Kammer et al., 2015; Bayart et al., 2016; Galis et al., 2017; Bayart et al., 2018; Gvirtzman and Fineberg, 2021; Cebry et al., 2022; Paglialunga et al., 2022). Here, the possible effects of preconditioning have been explored experimentally, demonstrating general agreement with previously-made predictions. In particular, preconditioning has been shown to be capable of slowing and/or halting a dynamically propagating rupture as well as reducing the slip and slip velocity behind the dynamically-propagating crack tip, resulting in a smaller seismic moment for nucleated events. This effect of preconditioning on rupture propagation can be principally the result of (i) the increase in the energy required to continue crack propagation (the fracture energy, G_c), (ii) the reduction of the mechanical energy flux at the crack tip (G), or (iii) a combination of both.

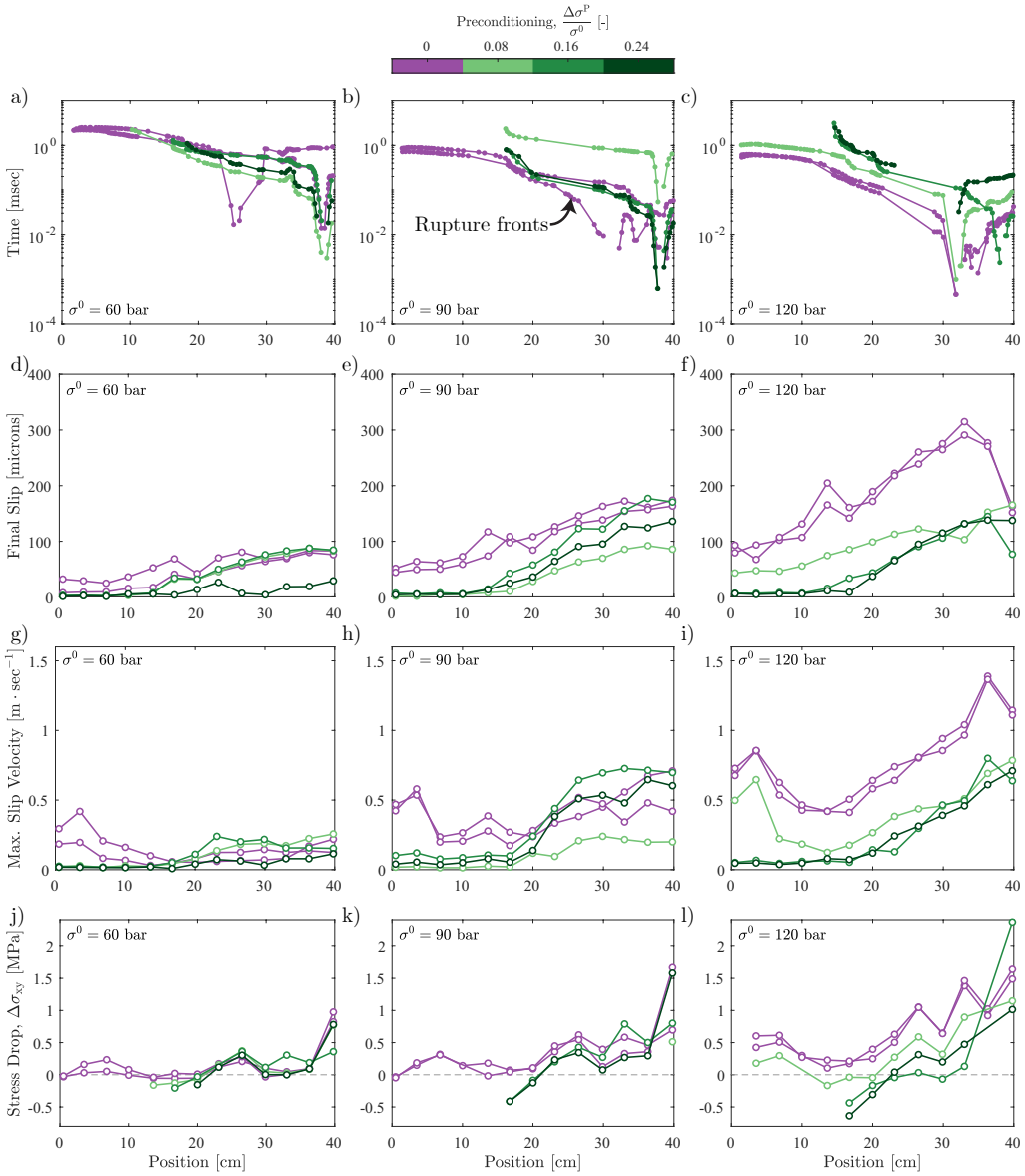

Figure 4: (a-c) The crack tip progression for each experiment, manually picked from videograms. Dots represent manually-picked points; linear interpolation is used between these points. (d-f) The total (maximum) slip calculated from the accelerometers, calculated up to 1.5 msec after the trigger. (g-i) The maximum slip velocity up to 1.5 msec after the trigger. For (d-i), white dots represent the locations of accelerometers; linear interpolation is used between these locations. (j-l) The stress drop resulting from the dynamic event calculated using the strain gauges. White dots represent the locations of strain gauge rosettes; linear interpolation is used between these locations. Stress drops are only plotted for positions behind the crack tip; however note that the strain gauge at 0.5 cm was not working for the experiments at 120 bar. Experiments are performed at (a,d,g,j) 60, (b,e,h,k) 90, and (c,f,i,l) 120 bar nominal normal stress. For all plots, the color bar indicates the amount of preconditioning used in each experiment.

4.1.1. *Influence of fault preconditioning on G_c*

The dependence of G_c on normal stress was examined through two calibration experiments, both exhibiting complete ruptures. The determination of G_c began with the calculation of the breakdown work, w_b, (Tinti et al., 2005; Brener and Bouchbinder, 2021b,a),

$$w_b(D) = \int_0^D \left(\sigma_{xy}(\delta) - \sigma_{xy}(D)\right) d\delta, \tag{2}$$

where $d\delta$ is an increment of slip. Note that the definition of breakdown work here is slightly modified from that introduced by Tinti et al. (2005) to follow Brener and Bouchbinder (2021b,a); Paglialunga et al. (2022, 2024), and is precisely the definition of fracture energy in Abercrombie and Rice (2005), stemming from Palmer and Rice (1973). The breakdown work was determined for multiple events at various strain gauge rosettes.

Initially, once the rupture tip first passes a specific location along the fault and slip initiates, breakdown work scales as $w_b \propto D^2$ (Tinti et al., 2005; Brener and Bouchbinder, 2021b); however, this phase is generally not seen here to due the frequency response of the accelerometers. At larger values of slip, the relationship between w_b and D undergoes a change, such that $w_b \propto D^m$, where m is a fitting parameter. The slip which corresponds to this change in dependence is known as the critical slip distance, D_c, and corresponds to a cross-over slip scale. Within the framework of LEFM, weakening is localized in an infinitesimal region near the crack tip, so that no further weakening occurs when $D \geq D_c$. This results in $w_b \propto D^0$ and corresponds to a singularity order, ξ, of -0.50 (e.g., Svetlizky et al. (2020); Shlomai et al. (2021); Brener and Bouchbinder (2021b)). The breakdown work achieved at $D = D_c$ is equivalent to the fracture energy, such that $G_c = w_b(D = D_c)$.

In these experiments, breakdown work is generally a continuously-increasing function of slip even when $D \geq D_c$, and can be fit as $w_b(D \geq D_c) = AD^m$, Figure 5b and appendix B, where A is a fitting parameter. There is therefore a cross-over behaviour occurring at $D = D_c$ from a small-slip behaviour where $w_b \propto D^2$ to a large-slip behaviour where $w_b \propto D^m$, as described by previous authors (Viesca and Garagash, 2015; Brantut and Viesca, 2017; Brener and Bouchbinder, 2021b; Paglialunga et al., 2024). The latter results in unconventional singularity orders in stress and strain, $\xi = \frac{m-1}{2-m}$, ranging between -0.52 and -0.18, with mean and median values of -0.28 and -0.24, respectively, appendix B. Such values depart from the "conventional" -0.5 value of LEFM and are close to the value -0.25 expected for flash heating (Brantut and Viesca, 2017; Brener and Bouchbinder, 2021b; Paglialunga et al., 2024) and thermal pressurization (Viesca and Garagash, 2015). In order to further confirm the presence of these unconventional singularity orders, the stress perturbations associated with passing rupture tips were fit to the ruptures' singular fields using both the unconventional singularity orders found from the trend between w_b and D and the conventional singularity order of $\xi = -0.50$ (Irwin (1957); Freund (1990), Eqn 4.3.23; Paglialunga et al. (2024), Eqns 7-9), appendix B. The use of unconventional singularity orders generally resulted in superior fits, Figure 5a, thereby providing further evidence for the unconventional nature of these singularities. These experimental results are a demonstration of the numerical prediction by Lambert and Lapusta (2020) that breakdown energy is "neither a constant material property nor uniquely defined by the amount of slip attained during the rupture" and builds upon previous discussions by, for example, Abercrombie and Rice (2005); Kammer et al. (2024) who considered the scale dependence of earthquake rupture.

The fitting of the singular field with the conventional singularity order of $\xi = -0.50$ further allows for the calculation of G_c^{LEFM} (e.g., Svetlizky et al. (2020)). This value of G_c^{LEFM} and the

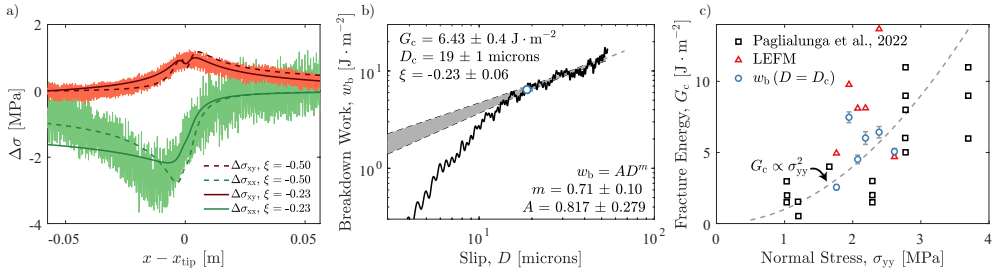

Figure 5: a) An example of the fitting (dark and dashed lines) of $K_{\text{II}}^{(\xi)}$ to the stress change seen by one strain gauge rosette (light lines, green for σ_{xx} and red for σ_{xy}) as the rupture front passes it. The dashed lines are fit as a conventional singularity with $\xi = -0.5$; the dark lines are fit as an unconventional singularity with $\xi = -0.23$. These data are from a calibration experiment and are filtered at 100 kHz. b) From the same experiment, the breakdown work plotted as a function of slip. After the trend between w_b and D turns over, becoming approximately linear in log-log space, it is fit as $w_b = AD^m$. The beginning of this trend corresponds to $D = D_c$ and $w_b(D = D_c) = G_c$ and is marked with a blue point. Further, the singularity order can then be calculated as $\xi = \frac{m-1}{2-m}$. The cross over in scaling at $D = D_c$ has been described by Viesca and Garagash (2015); Brantut and Viesca (2017); Brener and Bouchbinder (2021b); Paglialunga et al. (2024). c) The fracture energy, G_c, versus normal stress, σ_{yy}, based on calibration experiments performed for this study using either LEFM fits (triangles) or the change in trend between breakdown work and slip (circles). Data taken from Paglialunga et al. (2022) are also plotted (squares).

value of G_c found from the trend between w_b and D allow for the calibration of G_c's dependence on normal stress, Figure 5c and appendix C. G_c's dependence on normal stress has been previously demonstrated (Okubo and Dieterich, 1981, 1984; Bayart et al., 2016, 2018; Paglialunga et al., 2022), and the results here are in agreement with previous findings, Figure 5(c). Therefore, the increase in normal stress associated with pore pressure preconditioning is predicted to cause in an increase in fracture energy, resulting in a fracture energy barrier. These fracture energy barriers represent *local* impediments to propagation and have been previously shown to be capable of halting dynamically-propagating ruptures (Husseini et al., 1975; Bayart et al., 2016, 2018; Gvirtzman and Fineberg, 2021). It should be noted, however, that, for the normal stresses investigated here, G_c varies only from approximately 5 to 10 $\frac{\text{J}}{\text{m}^2}$, depending on whether the LEFM or breakdown-work-derived values are used. As will be demonstrated later, these results imply that fracture energy barriers do not exert the primary control on rupture arrest in these scenarios.

4.1.2. Influence of fault preconditioning on the energy flux, G

Complementary to this effect on the fracture energy, fault preconditioning is also expected to reduce the energy flux to the crack tip. In the case of rupture arrest during mode-II propagation in plane stress conditions (in the framework of LEFM - these equations are undefined for unconventional singularities), $\lim_{v\to 0} G = G^{\text{stat}}(a) = \frac{\left(K_{\text{II}}^{\text{stat}}(a)\right)^2}{E}$ (Freund (1990), Eqn. 5.3.10). The quantity $K_{\text{II}}^{\text{stat}}(a)$, the static mode-II stress intensity factor, can then be calculated explicitly as (Tada et al. (2000), Eqn. 8.3; Kammer et al. (2015); Bayart et al. (2016)),

$$K_{\text{II}}^{\text{stat}}(a) = \frac{2}{\sqrt{\pi a}} \int_0^a \frac{\Delta\sigma_{xy}(s)\, F\left(\frac{s}{a}\right)}{\sqrt{1 - \left(\frac{s}{a}\right)^2}} \mathrm{d}s, \tag{3}$$

where $F\left(\frac{s}{a}\right) = 1 + 0.297\left(1 - \left(\frac{s}{a}\right)^{\frac{5}{4}}\right)$, a is the crack length, and $\mathrm{d}s$ is an increment of crack length. In the frameworks of LEFM and cohesive zone models, the residual friction is often treated as a

local property of the interface (e.g., Bayart et al. (2016); Ke et al. (2018)), such that the residual shear stress can be predicted based on the known normal stress prior to the rupture. This enables the calculation of first $K_{\mathrm{II}}^{\mathrm{stat}}$ and then G^{stat} from the initial loading conditions. In the case of conventional singularities, this approach provides values of G^{stat} which show excellent agreement with observed rupture arrest when compared to G_{c} (e.g., Bayart et al. (2016, 2018); Ke et al. (2018)). However, in the case of the unconventional singularities observed here, the calculation of $\Delta\sigma_{\mathrm{xy}}$ is less clear. Behind the observed rupture arrest length, in an analogous fashion to LEFM, the measured stress drops (which, unlike for conventional-singularity-driven ruptures, include long-tailed weakening) might be taken after the shear stress achieves a relatively constant value. In front of the observed rupture arrest length, and again as in LEFM (e.g., Bayart et al. (2016); Ke et al. (2018)), an attempt might be made to predict the residual shear stress were the crack to pass a given location. The challenge arises from the fact that shear cracks driven by unconventional singularities do not present locally-constant values of residual friction. Consequently, variations in stress drop, slip, and rupture length are all interdependent, as observed in elastodynamics (e.g., Madariaga (2015)). Nevertheless, to adhere to a procedure typical of LEFM, an attempt was made to characterize the "residual" friction of the fault ahead of the observed rupture arrest length, and thereby predict the residual shear stress and stress drop that would result after the passing of a rupture front. This involved determining the "residual" friction of all complete ruptures, taking the median of this ensemble, and using this value to predict the stress drop that would have occurred for the contained ruptures were they to outgrow the location of their actual arrest. This residual friction profile therefore varies spatially and is assumed to be a local property of the interface.

This approach enables the estimation of G^{stat}, representative of the mechanical energy flux to the crack tip. G^{stat} is reduced during the preconditioning experiments, Figure 6(a-c), reflecting the reduction in energy flux when preconditioning is applied and occurring due to reduction in stress drop available to propagate the crack, Figure 4(j-l). This stress drop reduction, in turn, is due to the increase in the "residual" shear stress, appendix D. Due to the preconditioning phase, the normal stress distribution prior to rupture nucleation is increased from its *in-situ* value, while the shear stress distribution remains approximately unchanged, Figure 2(d,f). As the "residual" shear stress depends directly on the normal stress, this implies that the drop in shear stress available has been reduced by preconditioning. Indeed, preconditioning and stress barriers in general (i.e., local decreases in shear stress and/or local increases in normal stress) can even result in a negative stress drop, whereby shear stress is actually increased by the passing rupture, removing energy from the propagating crack tip, Figures 4(j-l). In fact, whether or not a stress drop is predicted to be negative or positive has been suggested numerous times as a criterion for dynamic rupture propagation (Garagash and Germanovich, 2012; Cebry et al., 2022), and is inherent in the LEFM framework (Freund (1990), Eqn 7.4.27; Bayart et al. (2016, 2018); Ke et al. (2018)) as a negative stress drop leads to a sharp decrease in energy release rate, see Figure 6(a-c). These stress drop barriers represent *global* impediments to rupture propagation as the stress drop across the entire interface of the slipping fault must be taken in to consideration. These experimental results highlight that pore pressure changes realistically achievable with pore pressure preconditioning (i.e., tens of percent of the normal stress) lead to relatively large changes in G^{stat} when compared to the potential changes in fracture energy, in conditions relevant for laboratory experiments (up to two orders of magnitude for G^{stat} compared to approximately a factor of four for G_{c}). Indeed, at x = 15 cm, a common position for rupture arrest, G_{c} is predicted to be increased by a factor of approximately two due to preconditioning, see appendix C. Conversely, at this position G^{stat} is increased by a factor of 10 and 100 for experiments at a nominal normal stress

of 90 and 120 bar, respectively. There is limited apparent effect for experiments performed at a nominal normal stress of 60 bar. Hence, the primary mechanism leading to the arrest of a rupture related to fault or reservoir preconditioning is the reduction of energy flux to the crack tip.

4.2. Influence of barrier size on rupture arrest

Our results demonstrated that fault preconditioning can halt potential seismic rupture propagation due to the reduction of the energy flux to the crack tip. However, several studies have shed light on ruptures skipping over spatially-limited barriers (Das and Aki, 1977; Cebry et al., 2023). The focus here has been principally placed on testing different magnitudes of pore pressure preconditioning, with $\frac{\Delta\sigma^{\mathrm{P}}}{\sigma^{0}} = 0.08, 0.16, 0.24$. However, as previously highlighted (Fryer et al., 2023), the extent of this barrier is also of significance. If the period of production leading to preconditioning is too short, the stress barrier may be large in magnitude, but will be small in extent. It is therefore possible that dynamically-propagating ruptures will be able to overcome these barriers and continue propagating. To illustrate this, preconditioning was only applied to one of the pistons (both central- and periphery-only preconditioning were tested, affecting approximately one third of the fault length), with the result compared to the base case where the entire sample interface is preconditioned, Figure 7. As can be seen, the ruptures in these cases are liable to skip past the barrier for low values of $\frac{\Delta\sigma^{\mathrm{P}}}{\sigma^{0}}$, highlighting the significance of achieving pore-pressure decreases which are not just large in magnitude, but also in extent. Stress drops behind the crack tip recorded 1 msec after the trigger were also used to reconstruct the $\frac{G^{\mathrm{stat}}}{G_{\mathrm{c}}}$ profiles of these events. Generally, good but imperfect agreement is achieved with theory as the case with preconditioning applied to only the left-most piston never achieves values of G^{stat} significantly lower than G_{c} and is the only case presented in which the rupture is not arrested, Figure 7a. Note further that the rupture renucleates beyond the preconditioning stress in the case that preconditioning is only applied to the middle piston, Figure 7b.

4.3. Can the effect of fault preconditioning on rupture length be predicted?

Following Barras et al. (2023), their equation 31, the arrest length, $\bar{L}_{\mathrm{arr}}$, of a crack-like rupture encountering a stress barrier can be predicted in the framework of LEFM for the case of homogeneous loading and constant residual friction by,

$$\bar{L}_{\mathrm{arr}} = -\frac{\bar{\mathrm{x}}_{\mathrm{b}}\bar{\tau}_{0}}{\bar{\tau}_{\mathrm{b}}}, \tag{4}$$

where $\bar{\mathrm{x}}_{\mathrm{b}} = \frac{\mathrm{x}_{\mathrm{b}}}{H}$ is the position of the barrier normalized by the damage zone, H, and $\bar{\tau}_{0}$ and $\bar{\tau}_{\mathrm{b}}$ are the dimensionless stress parameters outside and within the barrier,

$$\bar{\tau}_{0} = \frac{\frac{\sigma^{0}_{\mathrm{xy}}}{\sigma^{0}_{\mathrm{yy}}} - f_{\mathrm{r}}}{f_{\mathrm{p}} - f_{\mathrm{r}}}, \quad \bar{\tau}_{\mathrm{b}} = \frac{\frac{\sigma^{\mathrm{b}}_{\mathrm{xy}}}{\sigma^{\mathrm{b}}_{\mathrm{yy}}} - f_{\mathrm{r}}}{f_{\mathrm{p}} - f_{\mathrm{r}}}, \tag{5}$$

resulting in, for the dimensional form of arrest length,

$$L_{\mathrm{arr}} = \mathrm{x}_{\mathrm{b}}\frac{\sigma^{0}_{\mathrm{xy}} - f_{\mathrm{r}}\sigma^{0}_{\mathrm{yy}}}{\sigma^{\mathrm{b}}_{\mathrm{xy}} - f_{\mathrm{r}}\sigma^{\mathrm{b}}_{\mathrm{yy}}}. \tag{6}$$

Here, σ^{0}_{xy} and σ^{0}_{yy} are the shear and normal stresses in the zone outside the barrier, and $\sigma^{\mathrm{b}}_{\mathrm{xy}}$ and $\sigma^{\mathrm{b}}_{\mathrm{yy}}$ are the shear and normal stresses within the barrier, respectively. f_{p} and f_{r} are the peak and

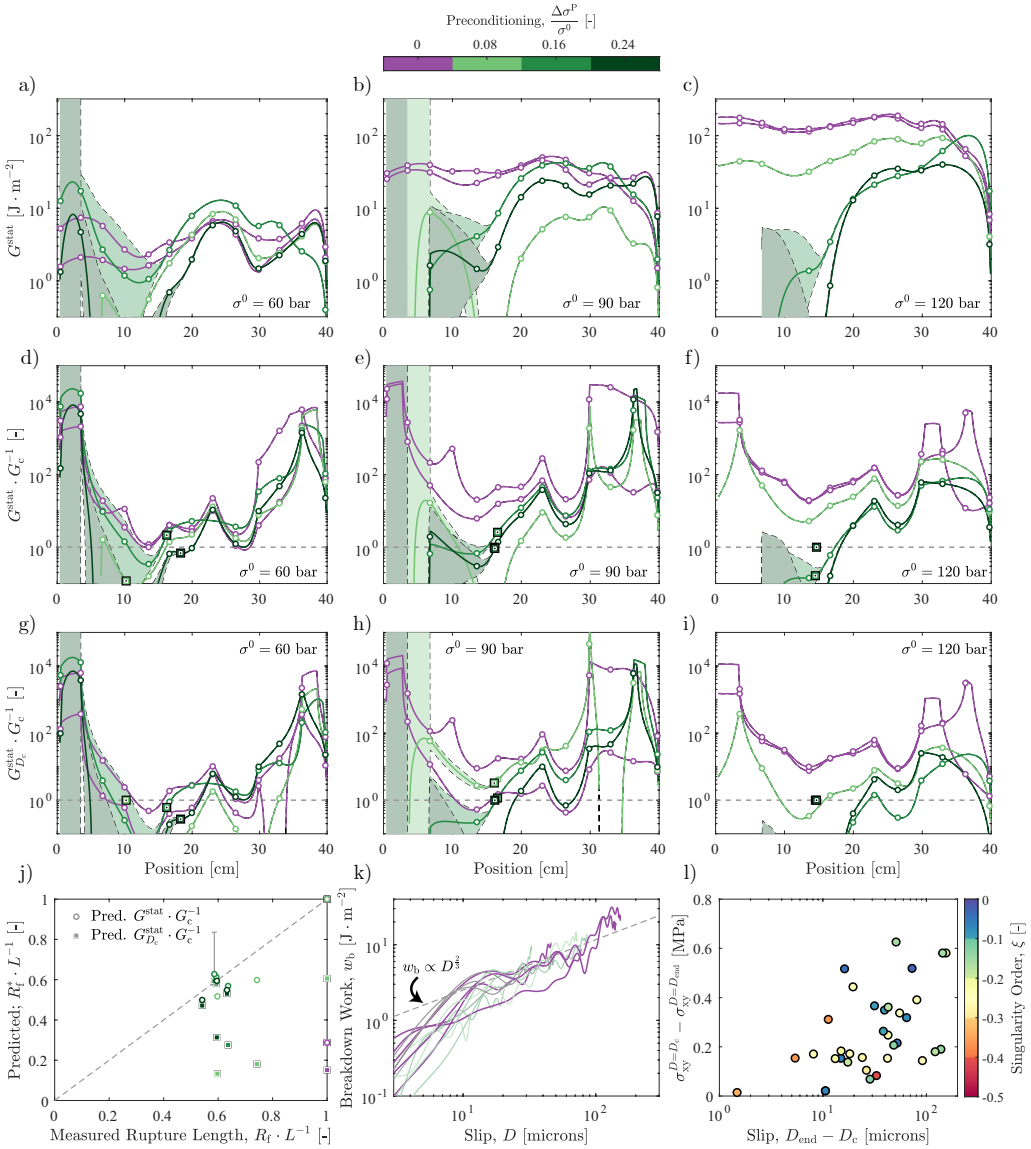
Preconditioning, $\frac{\Delta\sigma^{\mathrm{P}}}{\sigma^0}$ [-]
0
0.08
0.16
0.24
a)
b)
c)
d)
e)
f)
g)
h)
i)
$\sigma^0 = 60$ bar
$\sigma^0 = 90$ bar
$\sigma^0 = 120$ bar
G^{stat} [J · m^{-2}]
$G^{\mathrm{stat}} \cdot G_{\mathrm{c}}^{-1}$ [-]
$G^{\mathrm{stat}}_{D_{\mathrm{c}}} \cdot G_{\mathrm{c}}^{-1}$ [-]
Position [cm]
j)
k)
l)
Pred. $G^{\mathrm{stat}} \cdot G_{\mathrm{c}}^{-1}$
Pred. $G^{\mathrm{stat}}_{D_{\mathrm{c}}} \cdot G_{\mathrm{c}}^{-1}$
Predicted; $R_{\mathrm{f}}^* \cdot L^{-1}$ [-]
Measured Rupture Length, $R_{\mathrm{f}} \cdot L^{-1}$ [-]
Breakdown Work, w_{b} [J · m^{-2}]
$w_{\mathrm{b}} \propto D^{\frac{2}{3}}$
Slip, D [microns]
$\sigma_{xy}^{D=D_{\mathrm{c}}} - \sigma_{xy}^{D=D_{\mathrm{end}}}$ [MPa]
Slip, $D_{\mathrm{end}} - D_{\mathrm{c}}$ [microns]
Singularity Order, ξ [-]

residual friction coefficients, respectively. This equation represents a simplified approach with its use of unrealistic homogeneous stress values, see Figure 2. However, it may still provide a first-order estimate of the arrest length of the rupture. Considering that two out of the three pistons maintain their preconditioned load during the unloading of the third piston, the barrier position can be taken as one-third of the sample length, or approximately 13 cm. In the case that the nominal normal load is 120 bar, the shear stress can be taken as approximately 1.2 MPa, Figure 2(e,f). The normal load is more heterogeneous. At the moment of nucleation, in the case that $\sigma^0 = 120$ bar, the normal stress is approximately 0.8 MPa in the unloaded zone and 1.6 MPa in the barrier region. Finally, the measured residual friction is heterogeneous across the sample interface, but to a first order might be taken as 0.5. Crudely, this yields an arrest length estimate of 26 cm which is in agreement with the measured rupture lengths for the preconditioned cases, Figure 4(a-c). It should be emphasized, however, that there is a large degree of arbitrariness in this calculation, which inherently does not consider the large degree of heterogeneity along the sample interface, despite the tested material's synthetic nature and the highly-controlled laboratory environment. Indeed, for the experiments performed at a nominal normal stress of 120 bar without preconditioning, the normal stress in the barrier region is only marginally lower, Figure 2, yet this small discrepancy in normal stress is sufficient to enable complete rupturing in all cases which are not preconditioned. It is difficult to see how such fine margins could be accurately captured by an approach which does not incorporate heterogeneity. More success may be had applying this approach to either larger-scale or more extreme cases, where the stress conditions are not on the border between halting or encouraging rupture propagation.

Conversely, the approach of Section 4.1.2 integrates the heterogeneity present along the fault into its prediction of rupture halting and has been successful in this regard (e.g., Bayart et al.

Figure 6 *(preceding page)*: While Equation 3 can be used in the prediction of rupture arrest length using the full stress drop, the stress drop at $D = D_c$ does not provide satisfactory predictions. Therefore, in order to describe shear crack growth when driven by unconventional singularities for which energy dissipation is not exclusively located at the crack tip, continued weakening after $D = D_c$ must be incorporated; the consideration of energy dissipation localized in the vicinity of the rupture tip without the inclusion of tail processes is not sufficient. (a-c) The profiles of G^{stat} for each experiment. G^{stat} is based on a combination of the measured stress drop behind the ultimate crack tip arrest length and the predicted stress drop ahead of the ultimate observed crack tip arrest length. The prediction ahead of the ultimate crack tip arrest length is based on the median of the ensemble of residual friction values calculated from experiments without preconditioning, as these experiments exhibited complete ruptures, appendix D. The uncertainty bounds are based on the first and third quartile of the same ensemble of residual friction values. (d-f) The evolution of $\frac{G^{\text{stat}}}{G_c}$ for each experiment. G_c profiles are calculated based on the measured normal stress and the trend shown in Figure 5c. (g-i) The evolution of $\frac{G^{\text{stat}}_{D_c}}{G_c}$ based on the profiles of $G^{\text{stat}}_{D_c}$ built using the stress drop at $D = D_c$. Note that for certain strain gauges it was not possible to accurately pick D_c. At these strain gauges the full stress drop was used, such that $\frac{G^{\text{stat}}_{D_c}}{G_c}$ is overestimated. The friction profile used to predict stress drops ahead of the rupture tip was also built using the stress drop at $D = D_c$. (d-i) The position at which the rupture was arrested, based on the videograms, is shown with a square. Where possible the square is placed on the relevant $\frac{G^{\text{stat}}}{G_c}$ curve; otherwise it is placed at $\frac{G^{\text{stat}}}{G_c} = 1$. j) The predicted rupture length versus the measured rupture length for the cases that the energy flux is calculated using the full stress drop, G^{stat}, and the stress drop at $D = D_c$, $G^{\text{stat}}_{D_c}$. k) The breakdown work development with slip for all experiments based on a strain gauge rosette located outside the approximate point of nucleation (rosette located at x = 29.9 cm). Emphasis is placed on complete ruptures, with preconditioned experiments in a faded color. The ruptures from calibration experiments at the same rosette are shown in faded grey. The breakdown work for all calibration experiments can be found in the appendix B. l) The difference in residual shear stress at $D = D_c$ compared to when $D = D_{\text{end}}$ versus the slip occurring after $D = D_c$. D_{end} is the final value of slip. The color bar shows the inverted value of ξ, the singularity order of the rupture at the location of the strain gauge. Experiments performed at (a,d,g) 60, (b,e,h) 90, and (c,f,i) 120 bar nominal normal stress. (a-k) The color bar indicates the amount of preconditioning used in each experiment.

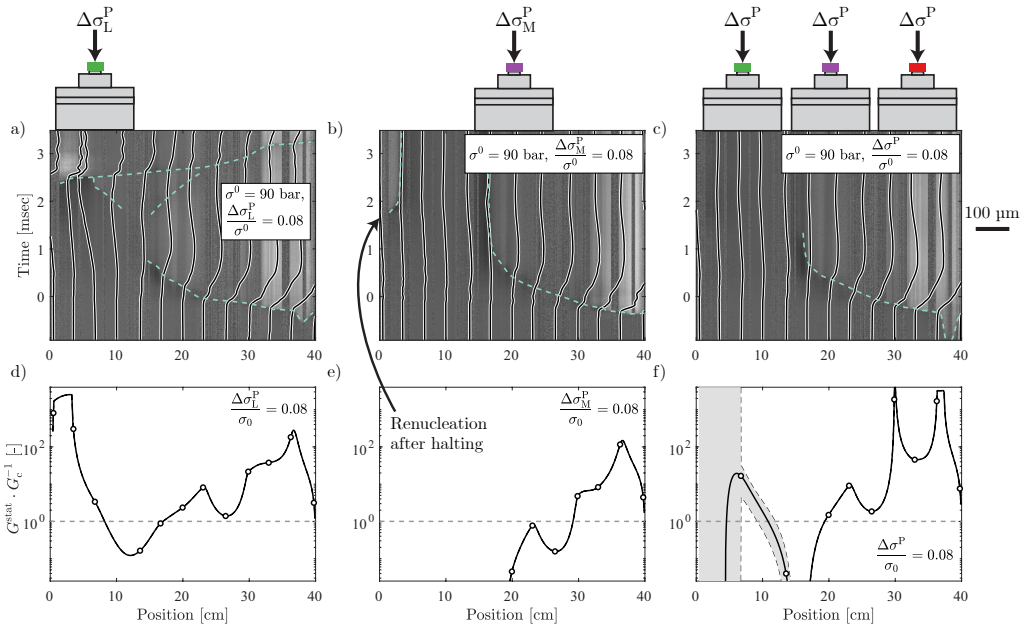

Figure 7: Three separate experiments, all performed at a nominal normal stress of 90 bar and a preconditioning stress of 7 bar. Unloading is performed only by the right-hand side piston. (a-c) The videogram illustrates the progression of the rupture front and is overlain by the local displacement recorded by the horizontally-oriented accelerometers (black lines). The scale for the displacement found from the accelerometers is found on the right. The rupture front is traced with a dotted teal line. Note that certain spatial bands where the grey-scale remains uniform on the videograms correspond to areas where light was not able to pass through the sample at the height of the fault. This is due to it being blocked by a sensor. (d-f) The ratio of G^{stat} to G_{c} calculated 1 msec after the trigger. As the ratio falls below one the rupture is predicted to halt. White dots mark the locations of strain gauge rosettes. (a,d) Preconditioning is only applied by the left-most piston. The rupture is initially slowed before accelerating again after approximately 2.5 msec. (b,e) Preconditioning is only applied to middle piston. The rupture is halted but is then able to jump past the barrier and reinitiate on the left-hand side of the sample. (c,f) Preconditioning is applied to all three pistons. The rupture is halted and does not reinitiate. Note that rupture halting is predicted in (f) despite the large values of $\frac{G^{\text{stat}}}{G_{\text{c}}}$ predicted on the left-hand side of the sample.

(2016, 2018); Ke et al. (2018)). However, unlike the predictions by Barras et al. (2023) and others (e.g., Kammer et al. (2015)), these approaches require the characterization of the residual friction (and therefore residual shear stress) along the entirety of the fault, and generally assume that the residual friction is a local interface property. This poses a problem for the case of unconventional singularities, where a steady-state residual friction is not reached and the amount of weakening and residual shear stress depend on the amount of slip, Figure 6(k,l). Interestingly, by considering the full stress drop in Equation 3, the calculation of G^{stat} yields satisfactory predictions of rupture arrest length when compared to G_{c}, Figure 6(d-f,j). Unfortunately, due to the continued weakening, the *a priori* predictions of these full stress drops is not obvious, with slip, rupture length, and stress drop being fully coupled.

One alternative possibility is to assume that the energy dissipation relevant for driving the rupture is exclusively located at the crack tip, in the process zone. If this were to be the case, it might be possible to characterize the interface's residual friction at $D = D_{\text{c}}$ such that *a priori* predictions could be performed. To test this assumption, the stress drop up to $D = D_{\text{c}}$ was used in Equation 3 to ultimately calculate the tip-localized static energy flux, $G^{\text{stat}}_{D_{\text{c}}}$. $G^{\text{stat}}_{D_{\text{c}}}$ is always less than or equal to G^{stat} due to continued long-tail weakening which occurs when $D > D_{\text{c}}$ (Lambert and Lapusta, 2020; Brener and Bouchbinder, 2021b,a; Paglialunga et al., 2022, 2024). Values of $G^{\text{stat}}_{D_{\text{c}}}$ were compared to G_{c} to predict crack arrest, Figure 6(g-i). This methodology under predicts ultimate crack length, Figure 6(j), implying that $G^{\text{stat}}_{D_{\text{c}}}$ is an under-prediction of the energy driving rupture propagation. The continued weakening occurring when $D > D_{\text{c}}$, Figure 6(k,l), which is not localized at the crack tip, therefore plays a significant role in the propagation of ruptures driven by unconventional singularities. Further, as this continued weakening must be considered when calculating the energy flux driving the crack tip, the characterization of a residual friction to be used in the *a priori* prediction of stress drop is difficult or even impossible for these ruptures as a true residual friction is not achieved even after $D \gg D_{\text{c}}$. Several weakening mechanisms are expected to induce long-tailed weakening (i.e. unconventional singularity orders), such as thermal pressurization (Viesca and Garagash, 2015), flash heating (Brantut and Viesca, 2017), and melt lubrication of the full fault interface (Di Toro et al., 2011). Therefore, long-tailed weakening may be a common phenomenon for natural earthquakes. Nevertheless, it cannot be excluded that the residual friction might reach a steady-state value after a large amount of slip such that an equilibrium between the heat production and the heat dissipation within the fault zone has been achieved (although this seems unlikely for thermal pressurization considering the relatively long time scale of fluid diffusion). If this steady state residual friction is attained, the singularity is expected to become conventional, allowing for predictions using LEFM. However, steady state will require large amounts of slip (>10 meters (Di Toro et al., 2011), likely corresponding to a large moment-magnitude, $M_{\text{w}} > 7$, earthquake), resulting in cohesive zones on the order of kilometers (considering slip velocities on the order of meters per second and rupture velocities of many hundreds of meters per second). These large sections the fault which do not achieve sufficient slip will not reach a steady state friction. This steady state is further unlikely to be achieved in the context of induced seismicity and smaller magnitude events as thermal slip equilibrium distances depend inversely on normal stress (Di Toro et al., 2011).

In order for fracture mechanics to one day provide *a priori* predictions of rupture arrest for unconventional singularities, it must account for this continued weakening (Brener and Bouchbinder, 2021b,a). Ideally, an equation of motion describing the propagation of the ruptures should be developed to replace the edge-localized Equation 1 for unconventional-singularity-driven ruptures. It may be that, in the case of rupture arrest, this equation of motion will lend itself to cases

where G_c can be neglected, potentially leading rupture propagation domains, such as a stress-drop-dominated domain, analogous to the zero-toughness asymptotic solutions for fluid-driven mode-I fractures (Savitski and Detournay, 2002). At any rate, it has been shown here that stress barriers not only affect the LEFM-defined parameters G_c and G, they also further reduce the breakdown work by reducing the slip and weakening (stress drop) occurring outside of the cohesive zone, thereby further reducing the energy flux propagating to the crack tip beyond what can be predicted by LEFM. Indeed, the events with the smallest amount of additional weakening when $D > D_c$ are those with the largest stress barriers. This additional, distal weakening has been shown to be significant for the accurate calculation of the energy flux to the crack tip. These results are even more relevant for induced seismicity, since shear ruptures propagating in the presence of fluids are inherently expected to be driven by unconventional singularities (i.e., even without the activation of thermal weakening, as for instance in the case of mode-I fractures), due to the diffusion of the fluid pressure along the fault and in the surrounding medium (Garagash et al., 2011).

4.4. Natural stress barriers and earthquake swarms

Heterogeneous pore pressure fields associated with some seismic swarms can induce stress barriers which can be used to explain changes in stress drop within the swarm without recourse to material or total-stress heterogeneity. Earthquake swarms are common in areas of volcanism and geothermal activity and occur such that the number and magnitude of earthquakes fluctuate in time whilst not presenting a distinct, larger-magnitude main shock (Mogi, 1963). Swarms have been previously suggested to be related to heterogeneous material properties and stress distributions (Mogi, 1963), with evidence from laboratory (Scholz, 1968) and earthquake monitoring (Ross et al., 2020) studies. For example, the 2016-2019 earthquake swarm near Cahuilla, California is thought to have been due to fluid influx and to be located along a fault with permeability barriers (Ross et al., 2020). In fact, before the occurrence of a moment magnitude, M_w, 4.4 earthquake, the swarm was seen to migrate in space and time, exhibiting progressively lower stress drops (Ross et al., 2020). While the influence of mechanical properties is likely in this case (Ross et al., 2020), for a constant shear stress (on the time scale of the fluid diffusion), a lower fluid pressure will result in an increased effective normal stress and, therefore, an increased "residual" shear stress, resulting in an ultimately lower stress drop, as has been shown in this work. Since the fluid source in this M_w 4.4 earthquake's case was thought to be coming from a point source (a broken seal connected to a deeper reservoir) (Ross et al., 2020), the earthquakes occurring farther from the point source were likely occurring in and/or propagating into zones of lower fluid pressure and therefore higher residual shear stress, offering an additional explanation for trends in stress drop seen for this swarm. It should be further noted that, as with injection-induced seismicity, fluid-driven earthquake swarms can be expected to be characterised by unconventional-singularity-driven ruptures due to their reliance on fluid pressure, making the results presented here particularly applicable.

5. Conclusion and Outlook

Preconditioning has been demonstrated experimentally, with stress changes that correspond to pore pressure changes which are reasonably achievable in the field. Preconditioning consistently results in rupture arrest at stress changes which correspond to pore pressure reductions of 2 $\frac{\text{MPa}}{\text{km}}$. All tested magnitudes of preconditioning (1, 2, and 3 $\frac{\text{MPa}}{\text{km}}$) result in reduced co-seismic

slip, slip velocity, stress drop, and seismic moment. However, these experiments were performed on analogue material at laboratory scales and stresses. Meso-scale testing could be pursued to test the influence of these limitations.

The experimental ruptures investigated here were driven by unconventional singularities, such that breakdown work continuously increased with slip. LEFM requires scale separation between edge-localized dissipation and linear elastic driving energy. The breakdown work increasing with slip breaks this scale separation as the energy dissipation is not exclusively localized near the crack tip (Brener and Bouchbinder, 2021b,a; Paglialunga et al., 2022, 2024). This makes the *a priori* use of a constant residual frictional coefficient to predict rupture arrest untenable. In order to precisely predict rupture arrest the full evolution of shear stress with slip must be considered, and an equation of motion for unconventional-singularity-driven ruptures should be developed. Here, ruptures which propagated into stress barriers were characterised by less slip and less weakening (stress drop) behind the crack tip. This means that stress barriers arrest ruptures by not just increasing the "residual" shear stress reached in the cohesive zone of the passing crack tip, they also reduce the long-tailed weakening occurring farther behind the crack tip by inhibiting slip and rupture advance. In summary, stress barriers increase fracture energy, reduce energy flux to the crack tip resulting from cohesive-zone weakening, and reduce energy flux to the crack tip resulting from distal, long-tailed weakening. All three of these effects aid in the arrest of the rupture and explain not only why preconditioning has the ability to reduce seismic hazard but also why natural fluid-driven earthquake swarms might exhibit lower stress drops away from the fluid source.

Acknowledgements

B.F., C.N., and both F.P.'s acknowledge funding from the European Union (ERC Starting Grant HOPE num. 101041966). B.F. acknowledges Hannes Hofmann for a useful discussion. The authors thank Julien Ambre for his help preparing sensors. Dmitry Garagash is thanked for helpful comments and suggestions.

Data availability

The data collected for this work and used in the analyses is publicly available (Fryer et al., 2024).

Appendix A. Tracking the rupture

Strain gauge data are filtered with a 6-th order low-pass Butterworth filter at 28 kHz, except for the fitting of the singular field where the filter is set to 100 kHz. The strain, ϵ_i, measured on

each strain gauge, i, is calculated as,

$$\epsilon_i = \frac{-4V_i}{V_{\text{ex}}\left(G_{\text{f}}G_{\text{amp}}\left(1+\frac{2V_i}{V_{\text{ex}}G_{\text{amp}}}\right)\right)}, \tag{A.1}$$

where V_i is the voltage measured by the i-th strain gauge, V_{ex} the excitation voltage, G_{f} the gauge factor, and G_{amp} the amplification gain. Depending on the orientation of the strain gauge from the vertical direction in degrees, these strains are referred to as ϵ_{315}, ϵ_0, and ϵ_{45}. These strains are then used to calculate the strain tensor at the location of the strain gauge rosette as,

$$\epsilon_{\text{xx}} = \epsilon_{315} + \epsilon_{45} - \epsilon_0, \quad \epsilon_{\text{yy}} = \epsilon_0, \quad \epsilon_{\text{xy}} = \frac{\epsilon_{45} - \epsilon_{315}}{2}. \tag{A.2}$$

The stress tensor was then calculated using Hooke's Law in plane stress, considering the strain rate dependence of the Young's Modulus of PMMA. A static Young's Modulus of 3.3 GPa and a dynamic Young's Modulus of 5.7 GPa were employed. Poisson's ratio was taken as 0.33, appropriate for PMMA. The static Young's Modulus was used to find all loading-phase stresses. The dynamic Young's Modulus was used to calculate the dynamic stress drop, following Bayart et al. (2016, 2018).

For each frame, the grayscale image recorded by the camera is taken as a 1280 x 32 matrix where the value ranges from zero (black) to a maximum value (white). The average greyscale map of the first 20 frames serve as a reference. All the future frames are compared to this reference in order to track stress changes along the interface and, therefore, track the rupture front position (e.g., Nielsen et al. (2010); Schubnel et al. (2011)).

The data from the accelerometers is converted from mV into $\frac{\text{m}}{\text{sec}^2}$ using the calibration provided by Brüel & Kjær. These accelerations are integrated twice in time to find both the velocity and displacement (e.g., Schubnel et al. (2011)). These data are unfiltered and multiplied by two, considering they represent movement on only one of the two similarly-sized blocks.

Appendix B. Characterizing dynamic rupture

To further confirm the presence of the unconventional singularity orders, the stress perturbation associated with a passing rupture can be described as (Irwin (1957); Freund (1990), Eqn 4.3.23; Paglialunga et al. (2024), Eqns 7-9),

$$\begin{aligned}
\Delta\sigma_{\text{xx}}(r,\theta) &= \frac{4(\xi+1)K_{\text{II}}^{(\xi)}}{\hat{D}\sqrt{2\pi}}\left[\alpha_{\text{s}}\left(1+2\alpha_{\text{d}}^2-\alpha_{\text{s}}^2\right)r_{\text{d}}^{\xi}\sin(\xi\theta_{\text{d}}) - \alpha_{\text{s}}\left(1+\alpha_{\text{s}}^2\right)r_{\text{s}}^{\xi}\sin(\xi\theta_{\text{s}})\right],\\
\sigma_{\text{xy}}(r,\theta) &= \sigma_{\text{xy}}^{\min} + \frac{2(\xi+1)K_{\text{II}}^{(\xi)}}{\hat{D}\sqrt{2\pi}}\left[4\alpha_{\text{s}}\alpha_{\text{d}}r_{\text{d}}^{\xi}\cos(\xi\theta_{\text{d}}) - \left(1+\alpha_{\text{s}}^2\right)^2 r_{\text{d}}^{\xi}\cos(\xi\theta_{\text{s}})\right],\\
\Delta\sigma_{\text{yy}}(r,\theta) &= \frac{4(\xi+1)\alpha_{\text{s}}\left(1+\alpha_{\text{s}}^2\right)K_{\text{II}}^{(\xi)}}{\hat{D}\sqrt{2\pi}}\left[r_{\text{d}}^{\xi}\sin(\xi\theta_{\text{d}}) - r_{\text{s}}^{\xi}\sin(\xi\theta_{\text{s}})\right],
\end{aligned} \tag{B.1}$$

where r and θ are polar coordinates centered on a steadily-moving crack tip, $K_{\text{II}}^{(\xi)}$ is the instantaneous mode-II stress intensity factor, $\hat{D} = 4\alpha_{\text{d}}\alpha_{\text{s}} - \left(1+\alpha_{\text{s}}^2\right)^2$ is the Rayleigh function (Freund (1990), Eqn 4.3.8), and $\alpha_{\text{d}} = \sqrt{1-(v/C_{\text{d}})^2}$ and $\alpha_{\text{s}} = \sqrt{1-(v/C_{\text{s}})^2}$ are velocity factors (Freund (1990), Eqn 4.3.12), where v is the rupture velocity and C_{d} and C_{s} are the P- and S-wave

Table B.1: Results of the fitting procedure used to find G_c described in the text. The ID contains the nominal normal stress of the calibration experiment, the the event number, and the strain gauge rosette number. σ_{yy} is the local normal stress measured by the strain gauges, v the local rupture velocity found from the videograms, l is the cohesive zone size and is found by choosing D_c on the plot of w_b vs. D (see main text for plot and Paglialunga et al. (2024), for example) and finding the time required to achieve this D_c since the passing of the rupture front. This time is multiplied by v (assumed constant) to yield l. The error in l is found based on the error in D_c (which affects the time to achieve D_c) and an assumed error of 10 $\frac{m}{sec}$ in v. Note that the uncertainty in l can be considered to be larger than the error presented here due to the sensitivity of l to other parameters. $G_c\,(D = D_c)$, D_c, and ξ are found from the plot of breakdown work versus slip.

ID	σ_{yy} [MPa]	v [$\frac{m}{sec}$]	$G_c\left(\xi = -\frac{1}{2}\right)$ [$\frac{J}{m^2}$]	l [cm]	D_c [μm]	$G_c\,(D = D_c)$ [$\frac{J}{m^2}$]	ξ [-]
200/1/11	1.95	214	9.77	1.2 ± 0.2	16 ± 3	7.47 ± 0.38	-0.24 ± 0.03
200/2/10	1.76	281	4.94	0.6 ± 0.2	9 ± 5	2.55 ± 0.18	-0.52 ± 0.04
200/2/11	2.07	178	8.10	1.3 ± 0.1	12 ± 1	4.51 ± 0.30	-0.24 ± 0.04
200/3/7	2.61	145	4.69	4.2 ± 0.3	19 ± 0	5.06 ± 0.22	-0.18 ± 0.25
200/3/11	2.19	159	8.12	1.6 ± 0.4	15 ± 5	6.01 ± 0.45	-0.27 ± 0.06
300/4/5	2.39	26	13.68	2.3 ± 1.0	19 ± 1	6.43 ± 0.40	-0.23 ± 0.06

velocities, respectively. σ_{yy} is positive in compression. The polar coordinates are corrected for distortion as $\theta_d = \arctan(\alpha_d \tan(\theta))$, $\theta_s = \arctan(\alpha_s \tan(\theta))$, $r_d = r\sqrt{1 - (v\sin(\theta)/C_d)^2}$, and $r_s = r\sqrt{1 - (v\sin(\theta)/C_s)^2}$ (Freund (1990), Eqn 4.3.12). σ_{xy}^{min} is the minimum value of shear stress achieved after the passing of the rupture. By fitting all three stress components to Equation B.1, $K_{II}^{(\xi)}$ can be found for each location along the fault with reliable strain gauge measurements. The singularity order, ξ, is -0.5 for conventional-singularity-driven shear cracks, which reduces Equation B.1 to the classical equations (Freund (1990), Eqn 4.3.23). Here, $K_{II}^{(\xi)}$ was fit with both $\xi = -0.5$ and the value of ξ found from the fitting of the trend between breakdown work to slip. The use of unconventional singularity orders generally resulted in superior fits, thereby providing further evidence for the unconventional nature of these singularities. Note that this inversion requires a constant rupture velocity. The variation in rupture velocities during these experiments may lead to error in the inversion.

The fits performed assuming a conventional singularity order (i.e., $\xi = -0.5$) were used to provide a point of comparison for the values of G_c found considering the trend between w_b and D. Following LEFM, G, which depends on the velocity of propagation, can be related to the the dynamic mode-II stress intensity factor, $K_{II}^{(\xi=-0.5)}$, as (Freund (1990), Eqn 5.3.10; Bayart et al. (2016)),

$$G(v) = \frac{\alpha\left(1 - \nu^2\right)}{E} f_{II}(v)\left[K_{II}^{(\xi=-0.5)}(a, v)\right]^2, \tag{B.2}$$

where $\alpha = 1$ in plane stress conditions, a is the crack length, and $f_{II}(v)$ is a decreasing function of velocity equivalent to (Freund (1990), Eqn 5.3.11),

$$f_{II}(v) = \frac{\alpha_s v^2}{\hat{D}(1 - \nu) C_s^2}, \tag{B.3}$$

having the property $\lim_{v \to 0} f_{II}(v) = 1$ (Freund (1990), page 234). Considering then that during dynamic rupture propagation $G = G_c$, the fit performed using Equation B.1 assuming $\xi = -0.5$, allows for the calculation of G_c. This value of G_c and the value of G_c found from the trend between w_b and D allow for the calibration of G_c's dependence on normal stress, Table B.1.

Appendix C. Dependence of the fracture energy G_c on normal stress

G_c depends on both the stress drop and the critical slip distance (Rice (1980), Chapter 5; Ohnaka (2003)) and therefore approximately quadratically with normal stress. Locally, both peak and residual shear stress vary linearly with normal stress, due to changes in real contact area (Bayart et al., 2016), with real contact area depending (sub-)linearly on normal stress (Bowden and Tabor, 1938; Archard, 1957). D_c can be estimated to vary linearly with normal stress assuming a constant rupture velocity and purely slip weakening behaviour (Ida, 1972; Palmer and Rice, 1973; Rice, 1980), with D_c's dependence on normal stress shown experimentally for PMMA (Paglialunga et al., 2022) and granite (Passelègue et al., 2016). Considering that fracture energy is estimated as $G_c = D_c\left(\sigma_{yy}\right)\sigma_{yy}\frac{f_p - f_r}{2}$ (e.g., Ida (1972); Palmer and Rice (1973); Rice (1980), Chapter 6; Okubo and Dieterich (1981, 1984)) in the linear slip weakening case, where f_p and f_r are the peak and residual friction coefficients, respectively, the result is that fracture energy is predicted to vary approximately quadratically with normal stress. This dependence could be even stronger as $f_p - f_r$ is also considered to scale with normal stress (Passelègue et al., 2016), for example through the activation of dynamic weakening mechanisms, such as flash heating (e.g., Brantut and Viesca (2017)), where residual friction is greatly reduced. It should be noted that K_{II}^{stat} also depends linearly on stress drop, implying a quadratic dependence of G^{stat} on normal stress in an LEFM framework. The activation of thermal weakening mechanisms at higher normal stresses, leading to long-tailed weakening, can be expected to further strengthen this dependence and may lead to a scale dependence in the relative importance of G^{stat} and G_c at higher normal stresses and longer rupture lengths. The measured normal stress and empirically-estimated fracture energy profiles are displayed in Figure C.8.

Appendix D. Residual shear stress

In these experiments, the residual shear stress is not a constant, nor a material property, Figure D.9. As described in the main text, normal stress barriers result in an increase in residual shear stress due to their ability to impede frictional rupture, thereby reducing distal weakening. Further, in a frictional setting the residual shear stress is generally thought as dependent on normal stress. As normal stress barriers represent zones of increased normal stress, the residual shear stress can be expected to be larger in these cases.

In order to predict the stress drop ahead of the ultimate crack length (i.e., in zones where the rupture did not pass and stress drop could therefore not be measured), the residual friction of the samples was characterized. This was done by taking the residual friction of all six non-preconditioned experiments as these experiments exhibited complete ruptures. The median and first and third quartile values of this ensemble, Figure D.10, were then used in combination with the measured normal and shear stresses to predict the stress drops of unruptured zones in the calculation of Equation 3. Note the edges of the sample exhibit large errors in residual friction due to the low values of normal stress present in these locations. Generally these areas are insignificant for rupture arrest prediction, as ruptures arrest typically between 10 and 20 cm.

References

Abercrombie, R., Rice, J., 2005. Can observations of earthquake scaling constrain slip weakening? Geophysical Journal International 162, 406–424. Https://doi.org/10.1111/j.1365-246X.2005.02579.x.

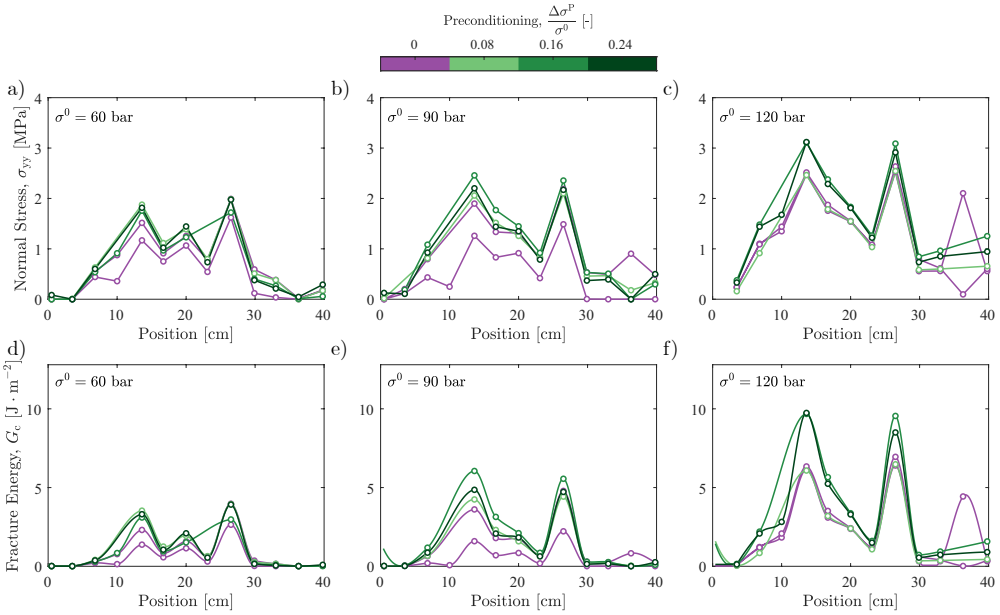

Figure C.8: (a-c) The normal stress measured by the strain gauges just before nucleation, found using the static Young's Modulus and limited to a minimum value of zero. (d-f) The predicted value of $G_c = \sigma_{yy}^2 + 0.001$ (with σ_{yy} in MPa) just before nucleation across the entire laboratory fault considering the measured normal stress. Experiments performed at (a,d) 60, (b,e) 90, and (c,f) 120 bar nominal normal stress. The color bar indicates the amount of preconditioning used in each experiment.

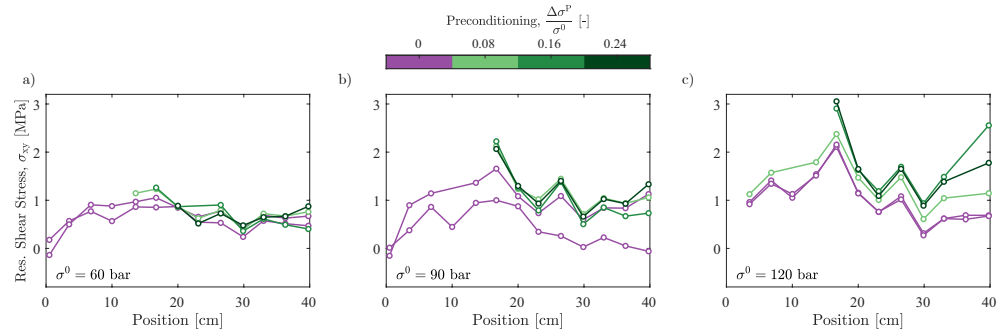

Figure D.9: The measured residual shear stress of each experiment, taken only for locations behind the arrested crack tip. Results for (a) 60, (b) 90, and (c) 120 bar nominal normal stress. The color bar indicates the amount of preconditioning used in each experiment.

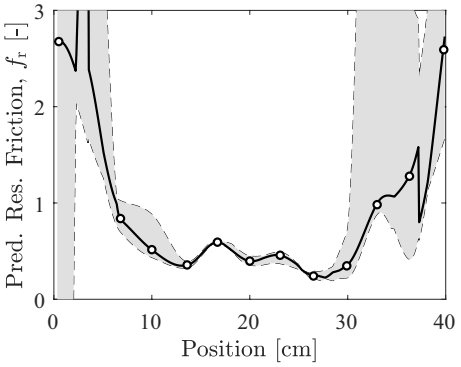

Figure D.10: The residual friction calculated based on all 6 non-preconditioned experiments, with estimated error shown as grey shading. The error and value of the residual friction are based on the first, second, and third quartile values of residual friction for the ensemble of experiments.

Aki, K., 1966. Generation and propagation of G waves from the Niigata Earthquake of June 16, 1964. Part 2. Estimation of earthquake moment, released energy, and stress-strain drop from the G wave spectrum. Bulletin of the Earthquake Research Institute 44, 73–88.

Archard, J., 1957. Elastic deformation and the laws of friction. Proceedings of the Royal Society of London Series A 243, 190–205. Https://dx.doi.org/10.1098/rspa.1957.0214.

Bao, X., Eaton, D., 2016. Fault activation by hydraulic fracturing in western Canada. Science 354, 1406–1409. Https://doi.org/10.1126/science.aag258.

Baria, R., Michelet, S., Baumgaertner, J., Dyer, B., Gerard, A., Nicholls, J., Hettkamp, T., Teza, D., Soma, N., Asanuma, H., Garnish, J., Megel, T., 2004. Microseismic monitoring of the World's largest potential HDR reservoir, in: Twenty-Ninth Workshop on Geothermal Reservoir Engineering Stanford University, Stanford, California, January 26-28, 2004.

Barras, F., Thøgersen, K., Aharonov, E., Renard, F., 2023. How do earthquakes stop? Insights from a minimal model of frictional rupture. Journal of Geophysical Research: Solid Earth 128. Https://doi.org/10.1029/2022JB026070.

Bayart, E., Svetlizky, I., Fineberg, J., 2016. Fracture mechanics determine the lengths of interface ruptures that mediate frictional motion. Nature Physics 12, 166–170. Https://doi.org/10.1038/nphys3539.

Bayart, E., Svetlizky, I., Fineberg, J., 2018. Rupture dynamics of heterogeneous frictional interfaces. Journal of Geophysical Research: Solid Earth 123, 3828–3848. Https://doi.org/10.1002/2018JB015509.

Ben-David, O., Cohen, G., Fineberg, J., 2010. The dynamics of the onset of frictional slip. Science 330, 211–214. Https://doi.org/10.1126/science.1194777.

Bhattacharya, P., Viesca, R., 2019. Fluid-induced aseismic fault slip outpaces pore-fluid migration. Science 364, 464–468. Https://doi.org/10.1126/science.aaw7354.

Bowden, F., Tabor, D., 1938. The area of contact between stationary and between moving surfaces. Proceedings of the Royal Society of London. Series A 169, 391–413. Https://doi.org/10.1098/rspa.1939.0005.

Brantut, N., Viesca, R., 2017. The fracture energy of ruptures driven by flash heating. Geophysical Research Letters 44, 6718–6725. Https://doi.org/10.1002/2017GL074110.

Brener, E., Bouchbinder, E., 2021a. Theory of unconventional singularities of frictional shear cracks. Journal of the Mechanics and Physics of Solids 153. Https://doi.org/10.1016/j.jmps.2021.104466.

Brener, E., Bouchbinder, E., 2021b. Unconventional singularities and energy balance in frictional rupture. Nature Communications 12. Https://doi.org/10.1038/s41467-021-22806-9.

Campillo, M., Ionescu, I., 1997. Initiation of antiplane shear instability under slip dependent friction. Journal of Geophysical Research 102, 20363–20371. Https://doi.org/10.1029/97JB01508.

Cebry, S., Ke, C., McLaskey, G., 2022. The role of background stress state in fluid-induced aseismic slip and dynamic rupture on a 3-m laboratory fault. Journal of Geophysical Research: Solid Earth 127. Https://doi.org/10.1029/2022JB024371.

Cebry, S., McLaskey, G., 2021. Seismic swarms produced by rapid fluid injection into a low permeability laboratory fault. Earth and Planetary Science Letters 557. Https://doi.org/10.1016/j.epsl.2020.116726.

Cebry, S., Sorhaindo, K., McLaskey, G., 2023. Laboratory earthquake rupture interactions with a high normal stress

bump. Journal of Geophysical Research: Solid Earth 128. Https://doi.org/10.1029/2023JB027297.
Clark, J., 1949. A hydraulic process for increasing the productivity of wells. Journal of Petroleum Technology 1. Https://doi.org/10.2118/949001-G.
Das, S., Aki, K., 1977. Fault plane with barriers: A versatile earthquake model. Journal of Geophysical Research 82, 5658–5670. Https://doi.org/10.1029/JB082i036p05658.
Di Toro, G., Han, R., Hirose, T., De Paola, N., Nielsen, S., Mizoguchi, K., Ferri, F., Cocco, M., Shimamoto, T., 2011. Fault lubrication during earthquakes. Nature 471, 494–498. Https://doi.org/.
Frash, L., Fu, P., Morris, J., Gutierrez, M., Neupane, G., Hampton, J., Welch, N., Carey, J., Kneafsey, T., 2021. Fracture caging to limit induced seismicity. Geophysical Research Letters 48. Https://doi.org/10.1029/2020GL090648.
Freund, L., 1990. Dynamic Fracture Mechanics. Cambridge University Press.
Fryer, B., Lebihain, M., Noël, C., Paglialunga, F., Passelègue, F., 2024. Data set for: The effect of stress barriers on unconventional-singularity-driven seismic rupture: An experimental demonstration of fault preconditioning". doi:10.5281/zenodo.13772819.
Fryer, B., Lebihain, M., Violay, M., 2023. Single-well pore pressure preconditioning for Enhanced Geothermal System stimulation. Journal of Geophysical Research: Solid Earth 128. Https://doi.org/10.1029/2022JB025443.
Fryer, B., Siddiqi, G., Laloui, L., 2020. Injection-induced seismicity: strategies for reducing risk using high stress path reservoirs and temperature-induced stress preconditioning. Geophysical Journal International 220, 1436–1446. Https://doi.org/10.1093/gji/ggz490.
Galis, M., Ampuero, J., Mai, P., Cappa, F., 2017. Induced seismicity provides insight into why earthquake ruptures stop. Science Advances 3. Https://doi.org/10.1126/sciadv.aap7528.
Garagash, D., 2021. Fracture mechanics of rate-and-state faults and fluid injection induced slip. Philosophical Transactions of the Royal Society A 379. doi:https://doi.org/10.1098/rsta.2020.0129.
Garagash, D., Detournay, E., Adachi, J., 2011. Multiscale tip asymptotics in hydraulic fracture with leak-off. Journal of Fluid Mechanics 669, 260–297. doi:10.1017/S002211201000501X.
Garagash, D., Germanovich, L., 2012. Nucleation and arrest of dynamic slip on a pressurized fault. Journal of Geophysical Research 117. doi:https://doi.org/10.1029/2012JB009209.
Gounon, A., Latour, S., Letort, J., El Arem, S., 2022. Rupture nucleation on a periodically heterogeneous interface. Geophysical Research Letters 49. Https://doi.org/10.1029/2021GL096816.
Griffith, A., 1921. Vi. the phenomena of rupture and flow in solids. Philosophical Transactions of the Royal Society of London. Series A, Containing Papers of a Mathematical or Physical Character 221, 163–198. Https://doi.org/10.1098/rsta.1921.0006.
Gvirtzman, S., Fineberg, J., 2021. Nucleation fronts ignite the interface rupture that initiates frictional motion. Nature Physics 17, 1037–1042. Https://doi.org/10.1038/s41567-021-01299-9.
Häring, M., Schanz, U., Ladner, F., Dyer, B., 2008. Characterisation of the Basel 1 enhanced geothermal system. Geothermics 37, 469–495. Https://doi.org/10.1016/j.geothermics.2008.06.002.
Hofmann, H., Zimmermann, G., Farkas, M., Huenges, E., Zang, A., Leonhardt, M., Kwiatek, G., Martinez-Garzon, P., Bohnhoff, M., Min, K., Fokker, P., Westaway, R., Bethmann, F., Meier, P., Yoon, K., Choi, J., Lee, T., Kim, K., 2019. First field application of cyclic soft stimulation at the Pohang Enhanced Geothermal System stie in Korea. Geophysical Journal International 217, 926–949. Https://doi.org/10.1093/gji/ggz058.
Hubbert, M., Willis, D., 1957. Mechanics of hydraulic fracturing. Petroleum Transactions, AIME 210, 153–168.
Husseini, M., Jovanovich, D., Randall, M., Freund, L., 1975. The fracture energy of earthquakes. Geophysical Journal International 43, 367–385. Https://doi.org/10.1111/j.1365-246X.1975.tb00640.x.
Ida, Y., 1972. Cohesive force across the tip of a longitudinal-shear crack and Griffith's specific surface energy. Journal of Geophysical Research 77. Https://doi.org/10.1029/JB077i020p03796.
Irwin, G., 1957. Analysis of stresses and strains near the end of a crack traversing a plate. Journal of Applied Mechanics 24, 361–364. Https://doi.org/10.1115/1.4011547.
Jalali, M., Selvadurai, P., Dal Zilio, L., Durand, V., Obermann, A., Meier, M., Amann, F., Zappone, A., Shakas, A., Rinaldi, A., Maurer, H., Bröker, K., Hertrich, M., Doonechaly, N., Achtziger-Zupancic, P., Wenning, Q., Ma, X., Cocco, M., Wiemer, S., Giardini, D., 2023. An attempt to control induced seismicity and on-fault stress pre-conditioning in the Bedretto Underground Laboratory, Switzerland, in: Proceedings: EGU General Assembly 2023, Vienna, Austria, 24–28 Apr 2023.
Kammer, D., McLaskey, G., Abercrombie, R., Ampuero, J., Cattania, C., Cocco, M., Dal Zilio, L., Dresen, G., Gabriel, A., Ke, C., Marone, C., Selvadurai, P., Tinti, E., 2024. Earthquake energy dissipation in a fracture mechanics framework. Nature Communications 15. Https://doi.org/10.1038/s41467-024-47970-6.
Kammer, D., Radiguet, M., Ampuero, J., Molinari, J., 2015. Linear elastic fracture mechanics predicts the propagation distance of frictional slip. Tribology Letters 57. Https://doi.org/.
Ke, C., McLaskey, G., Kammer, D., 2018. Rupture termination in laboratory-generated earthquakes. Geophysical Research Letters 45, 12784–12792. Https://doi.org/10.1029/2018GL080492.
Kilgore, B., McGarr, A., Beeler, N., Lockner, D., 2017. Earthquake source properties from instrumented laboratory

stick-slip, in: Thomas, M., Mitchell, T., Bhat, H. (Eds.), Fault Zone Dynamic Processes: Evolution of Fault Properties During Seismic Rupture, Geophysical Monograph. John Wiley & Sons, Inc.. chapter 8, pp. 151–169.
Kim, K., Ree, J., Kim, Y., Kim, S., Kang, S., Seo, W., 2018. Assessing whether the 2017 M_w 5.4 Pohang earthquake in South Korea was an induced event. Science 360, 1007–1009. Https://doi.org/10.1126/science.aat6081.
Lambert, V., Lapusta, N., 2020. Rupture-dependent breakdown energy in fault models with thermo-hydro-mechanical processes. Solid Earth 11, 2283–2302. Https://doi.org/10.5194/se-11-2283-2020.
Latour, S., Schubnel, A., Nielsen, S., Madariaga, R., Vinciguerra, S., 2013. Characterization of nucleation during laboratory earthquakes. Geophysical Research Letters 40, 5064–5069. Https://doi.org/10.1002/grl.50974.
Lee, H., Cho, T., 2002. Hydraulic characteristics of rough fractures in linear flow under normal and shear load. Rock Mechanics and Rock Engineering 35, 299–318. Https://doi.org/10.1007/s00603-002-0028-y.
Madariaga, R., 2015. Seismic Source Theory, in: Treatise on Geophysics, Second Edition. Elsevier B.V.. chapter 4, pp. 51–71.
Mogi, K., 1963. Some discussions on aftershocks, foreshocks and earthquake swarms - the fracture of a semi-infinite body caused by an inner stress origin and its relation to the earthquake phenomena (3rd paper). Bulletin of the Earthquake Research Institute 41, 615–658.
Nielsen, S., Taddeucci, J., Vinciguerra, S., 2010. Experimental observation of stick-slip instability fronts. Geophyscial Journal International 180, 697–702. Https://doi.org/10.1111/j.1365-246X.2009.04444.x.
Noël, C., Passelègue, F., Giorgetti, C., Violay, M., 2019. Fault reactivation during fluid pressure oscillations: Transition from stable to unstable slip. Journal of Geophysical Research: Solid Earth 124. Https://doi.org/10.1029/2019JB018517.
Ohnaka, M., 2003. A constitutive scaling law and a unified comprehension for frictional slip failure, shear fracture of intact rock, and earthquake rupture. Journal of Geophysical Research 108. Https://doi.org/10.1029/2000JB000123.
Okubo, P., Dieterich, J., 1981. Fracture energy of stick-slip events in a large scale biaxial apparatus. Geophysical Research Letters 8, 887–890. Https://doi.org/10.1029/GL008i008p00887.
Okubo, P., Dieterich, J., 1984. Effects of physical fault properties on frictional instabilities produced on simulated faults. Journal of Geophysical Research 89, 5817–5827.
Paglialunga, F., Passelègue, F., Brantut, N., Barras, F., Lebihain, M., Violay, M., 2022. On the scale dependence in the dynamics of frictional rupture: Constant fracture energy versus size-dependent breakdown work. Earth and Planetary Science Letters 584. Https://doi.org/10.1016/j.epsl.2022.117442.
Paglialunga, F., Passelègue, F., Latour, S., Gounon, A., Violay, M., 2023. Influence of viscous lubricant on nucleation and propagation of frictional ruptures. Journal of Geophysical Research: Solid Earth 128. Https://doi.org/10.1029/2022JB026090.
Paglialunga, F., Passelègue, F., Lebihain, M., Violay, M., 2024. Frictional weakening leads to unconventional singularities during dynamic rupture propagation. Earth and Planetary Science Letters 626. Https://doi.org/10.1016/j.epsl.2023.118550.
Palmer, A., Rice, J., 1973. The growth of slip surfaces in the progressive failure of over-consolidated clay. Proc. R. Soc. Lond. A 332, 527–548. Https://doi.org/10.1098/rspa.1973.0040.
Passelègue, F., Schubnel, A., Nielsen, S., Bhat, H., Deldicque, D., Madariaga, R., 2016. Dynamic rupture processes inferred from laboratory microearthquakes. Journal of Geophysical Research: Solid Earth 121, 4343–4365. Https://doi.org/10.1002/2015JB012694.
Pratt, W.E., Johnson, D.W., 1926. Local subsidence of the Goose Creek oil field. The Journal of Geology 34, 577–590.
Raleigh, C., Healy, J., Bredehoeft, J., 1976. An experiment in earthquake control at Rangely, Colorado. Science Https://doi.org/10.1126/science.191.4233.1230.
Rice, J., 1980. The mechanics of earthquake rupture, in: Dziewonski, A., Boschi, E. (Eds.), Physics of the Earth's Interior. Società Italiana di Fisica, Bologna, Italy, pp. 555–649.
Rosakis, A., Samudrala, O., Coker, D., 1999. Cracks faster than the shear wave speed. Science 284, 1337–1340. Https://doi.org/10.1126/science.284.5418.1337.
Ross, Z., Cochran, E., Trugman, D., Smith, J., 2020. 3D fault architecture controls the dynamism of earthquake swarms. Science 368, 1357–1361. Https://doi.org/10.1126/science.abb0779.
Roux, A., Leeman, E., Denkhaus, H., 1957. De-stressing: a means of ameliorating rockburst conditions. Part I—The concept of de-stressing and the results obtained from its application. The Journal of The South African Institute of Mining and Metallurgy , 101–119.
Savitski, A., Detournay, E., 2002. Propagation of a penny-shaped fluid-driven fracture in an impermeable rock: asymptotic solutions. International Journal of Solids and Structures 39, 6311–6337. Https://doi.org/10.1016/S0020-7683(02)00492-4.
Scholz, C., 1968. The frequency-magnitude relation of microfracturing in rock and its relation to earthquakes. Bulletin of the Seismological Society of America 58, 399–415.
Schubnel, A., Nielsen, S., Taddeucci, J., Vinciguerra, S., Rao, S., 2011. Photo-acoustic study of subshear and supershear ruptures in the laboratory. Earth and Planetary Science Letters 308, 424–432.

Https://dx.doi.org/10.1016/j.epsl.2011.06.013.
Shlomai, H., Kammer, D., Adda-Bedia, M., Arias, R., Fineberg, J., 2021. Unstable cracks trigger asymptotic rupture models in bimaterial friction. Journal of the Mechanics and Physics of Solids 149. Https://doi.org/10.1016/j.jmps.2021.104330.
Shuck, L., 1977. Method for selectively orienting induced fractures in subterranean Earth formations. U.S. Patent No. 4005750.
Stefanou, I., Tzortzopoulos, G., 2022. Preventing instabilities and inducing controlled, slow-slip in frictionally unstable systems. Journal of Geophysical Research: Solid Earth 127. Https://doi.org/10.1029/2021JB023410.
Svetlizky, I., Albertini, G., Cohen, G., Kammer, D., Fineberg, J., 2020. Dynamic fields at the tip of sub-Rayleigh and supershear frictional rupture fronts. Journal of the Mechanics and Physics of Solids 137. Https://doi.org/10.1016/j.jmps.2019.103826.
Tada, H., Paris, P., Irwin, G., 2000. The Stress Analysis of Cracks Handbook, Third Edition. ASME Press.
Tinti, E., Spudich, P., Cocco, M., 2005. Earthquake fracture energy inferred from kinematic rupture models on extended faults. Journal of Geophysical Research 110. Https://doi.org/10.1029/2005JB003644.
Uenishi, K., Rice, J., 2003. Universal nucleation length for slip-weakening rupture instability under nonuniform fault loading. Journal of Geophysical Research 108. Https://dx.doi.org/10.1029/2001JB001681.
Viesca, R., Garagash, D., 2015. Ubiquitous weakening of faults due to thermal pressurization. Nature Geoscience 8, 875–879. Https://doi.org/10.1038/NGEO2554.
Zang, A., Yoon, J., Stephansson, O., Heidbach, O., 2013. Fatigue hydraulic fracturing by cyclic reservoir treatment enhances permeability and reduces induced seismicity. Geophysical Journal International 195, 1282–1287. Https://doi.org/10.1093/gji/ggt301.
Zimmermann, G., Moeck, I., Blöcher, G., 2010. Cyclic waterfrac stimulation to develop an Enhanced Geothermal System EGS-Conceptual design and experimental results. Geothermics 39, 59–69. Https://doi.org/10.1016/j.geothermics.2009.10.003.